POLITECNICO DI TORINO

**Corso di Laurea Magistrale
in Ingegneria Energetica e Nucleare**

Tesi di Laurea Magistrale

ARC blanket: CFD and Tritium transport analysis

Relatori   **Candidato**

Prof. Massimo Zucchetti   Gabriele Ferrero
Dr. Raffaella Testoni

Co-relatore

Samuele Meschini

Marzo 2021

Sommario

Lo sviluppo di una centrale a fusione nucleare raccoglie gli sforzi e la ricerca dei paesi industrializzati di tutto il mondo: queste, infatti, potrebbero produrre energia pulita, senza emissioni di CO_2. Lo sviluppo di questa tecnologia si propone di superare sfide tecnologiche di notevole entità e varietà. Uno dei progetti di reattore a fusione più ambiziosi e innovativi è quello sostenuto dal Massachusetts Institute of Technology e dal Plasma Science and Fusion Center, il reattore ARC: Affordable Robust and Compact.

Lo scopo della seguente tesi lo sviluppo di un modello termofluidodinamico dettagliato, a regime stazionario, di ARC a partire dal progetto originario: in questo verrà analizzato in particolare il vacuum vessel e il breeding blanket, composto interamente dal sale fuso FLiBe, per osservarne il comportamento e individuarne le criticità. Data la complessità della geometria del reattore è difficile ottenere alcuni risultati con la precisione necessaria senza una simulazione CFD.

Inoltre, partendo dai risultati dello studio CFD svolto, viene fatta un'analisi del trasporto di Trizio nei medesimi componenti supportata da una simulazione tramite COMSOL Multiphysics. Lo studio del trasporto del Trizio è fondamentale per i reattori a fusione, e lo sviluppo di un breeding blanket che ne permetta la produzione ed estrazione è uno degli scogli più grandi per la realizzazione di un impianto commerciale.

Il campo di velocità e temperatura in ARC è stato calcolato. Viene proposta una configurazione alternativa degli ingressi del FLiBe, accompagnata da un paragone con la configurazione originale sottolineandone i miglioramenti. I risultati mostrano dei vortici nel breeding blanket, che possono determinare talvolta delle zone di surriscaldamento nel FLiBe e nel vessel. Lo scambio termico convettivo tra vessel e FLiBe sembra insufficiente e determina temperature critiche nello strato di Inconel 718 più interno. Il modello di trasporto del Trizio mostra una maggiore concentrazione localizzata in concomitanza dei vortici di FLiBe, ma la concentrazione più alta si osserva negli strati di Inconel 718, ordini di grandezza più alta che in tutti gli altri materiali di ARC.

Il modello sviluppato, oltre ad evidenziare alcune criticità del design attuale e a proporre un design alternativo, potrà essere usato come punto di partenza per modelli più precisi, includendo i fenomeni di MHD e l'evoluzione nel tempo.

Abstract

The development of a nuclear fusion plant gathers the efforts and the research of industrial countries from all over the world: these plants, indeed, could produce clean energy, without CO_2 emissions. The development of this technology means overcoming big technological challenges for many of the components. One of the most ambitious and innovative fusion reactor projects is under development at the Massachusetts Institute of Technology and Plasma Science and Fusion Center, with the name of ARC: Affordable, Robust and Compact.

The final goal for this thesis work is the development of a detailed steady-state CFD model of ARC. The model focuses on the vacuum vessel and on the innovative molten salt breeding blanket, to observe involved phenomena and to detect criticalities. It is difficult indeed to obtain precise results without a CFD simulation of the blanket, because of the complexity of its geometry.

Moreover, starting from CFD results, a Tritium transport analysis has been carried out in the same components with the support of a COMSOL Multiphysics transport model. Tritium transport study is fundamental for fusion reactors, and the development of a working breeding blanket that can produce and extract Tritium is one of the biggest obstacles for the realization of a commercial fusion power plant.

Flow field and temperature field in ARC has been determined. A different inlet configuration has been proposed and a comparison between original and new configuration has been carried, highlighting the improvements. Results showcased recirculating flows in the breeding blanket, sometimes leading to hotspots in FLiBe and in the vessel. Convective heat transfer between the vessel and FLiBe seems insufficient and leads to critical temperatures in the inner Inconel 718 layer. Tritium transport model evidenced a high concentration in recirculating flows, but the highest concentration is in Inconel 718 layers, orders of magnitude greater than any other ARC material.

The developed models evidence some criticalities on the current design; therefore, alternative solutions are proposed. Moreover, the models could be used as starting point for more detailed analyses that include MHD phenomena and time dependency.

Contents

1   Introduction to Fusion Reactors

Fusion reactors can be the energy source of the future: the main attractive aspect in fusion-powered reactors is the absence of emissions in the atmosphere. The comparison with traditional energy sources and in particular with fission reactors showcases that the advantages of fusion reactors[1], [2] are the following:

- No CO_2 and NO_x emissions, no greenhouse gases emitted;
- No power divergence unlike fission reactors; the fusion reaction needs to be boosted, unlike fission reactors that need to be restrained;
- Fuel cycle in situ: Tritium production and Deuterium reaction can be handled in situ, also reducing proliferation risks;
- Fuel abundance: Deuterium and Lithium are present enough in our planet;
- High energy density: fuel consumption is not a big issue (aside from Tritium) as fusion energy density is four times more than Uranium fission;
- Reduced radioactive wastes with respect to fission reactors: no high-level wastes are produced in a fusion reactor;

However, the main disadvantage is the feasibility of a commercial fusion reactor, which include extreme technological challenges, extreme operational conditions, fuel economy and a lot of effort in research and development[2]. Despite the huge technological challenges, nuclear fusion can contribute to a sustainable energy mix and to fight climate change. For these reasons, there is a vast scientific community carrying out projects like ITER [3], DEMO [4], and other smaller projects such as ARC [5], which is the subject of this thesis and will be further analyzed in paragraph 1.3.

1.1   Fusion Reaction

Nuclear fusion is a nuclear reaction where two colliding nuclei merge into different nuclei with great release of energy, as the product's mass is smaller than the reactants. For this phenomenon to happen, two light nuclei with enough kinetic energy to overcome Coulomb forces between them must collide. As these repulsive forces are a great obstacle to overcome, the most interesting fusion reaction today is the D-T reaction, because of its lower threshold in comparison to other fusion reactions," only" 1 keV (11 million K) (Figure 1.1). The predominant state of matter at these high temperatures is plasma, a condition where all particles are ionized due to the high kinetic energy while maintaining a neutral charge overall.

Deuterium and Tritium are two Hydrogen isotopes: Deuterium is a stable isotope, it can be found in nature, and it can be extracted from water by isotope separation; Tritium instead is unstable and it cannot be found in nature. However, it is possible to produce Tritium starting from Lithium and a neutron source; this very delicate process will be handled in situ, and the fusion reactor itself acts as a neutron source.

According to Reaction 1, Deuterium and Tritium collide producing an α particle and a neutron. Product's energy is split between the two particles in the form of kinetic energy. While α particle energy is used to keep the plasma's temperature hot, neutron energy (approximatively 4/5 of total energy) can be extracted. As Tritium is radioactive and the outgoing neutron can activate materials, radioactivity is a concern in D-T fusion reaction.

$$D + T \rightarrow {}^4He + n + 17,6 \; MeV \;\; (1)$$
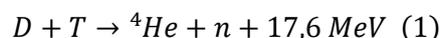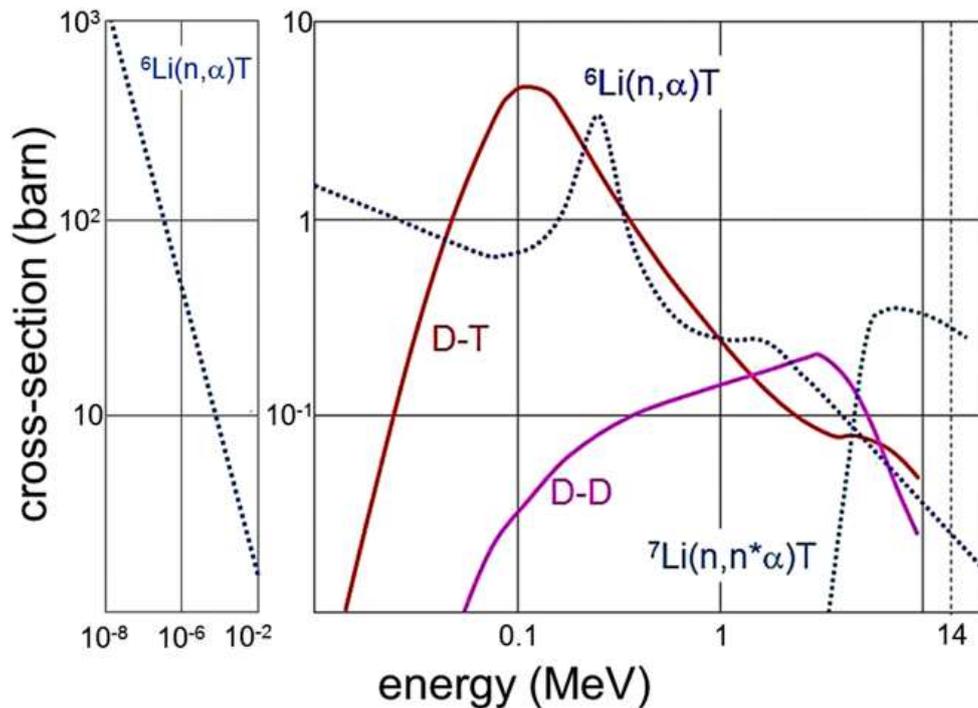
Figure 1.1 - D-T reaction scheme b) Fusion reactions cross sections and threshold temperatures [6].

1.2   Tokamaks

There are two reasons why plasma for fusion reaction must be confined avoiding direct contact with structural materials: structural materials interacting with plasma experience extremely intense heat loads and sputtering; on the other hand, the plasma itself turns off if it interacts heavily with solid materials because heavy nuclei from impurities irradiate energy cooling the plasma. Fusion reaction in nature is the power source of stars, and the confinement is provided by gravity; artificial fusion reactors will confine high-energy particles with magnetic confinement, as these charged particles gyrate following the magnetic field. There are two principal configurations of magnetic fields to confine plasma, the tokamaks and the stellarators[1]. In this work the main interest is in tokamaks as they result simpler to assemble and have a better performance. Tokamaks have two principal components of magnetic field, toroidal and poloidal, resulting into a torus-shaped configuration.

To provide stability and confinement to the plasma high magnetic fields are fundamental (from 3.5 T for JET[7] to 10-15 T for big magnets like "ITER model coil"[1]) (Figure 1.2). Superconducting magnets are the best technology to produce them because they can withstand enormous currents (7.5 MA [8]) without high Joule dissipation, that would probably make the energy production of the reactor worthless. As a tradeoff however, superconductive magnets are very susceptible to heat deposition and neutron damage and to work as intended they must be cooled below the temperature of the order of 5K.
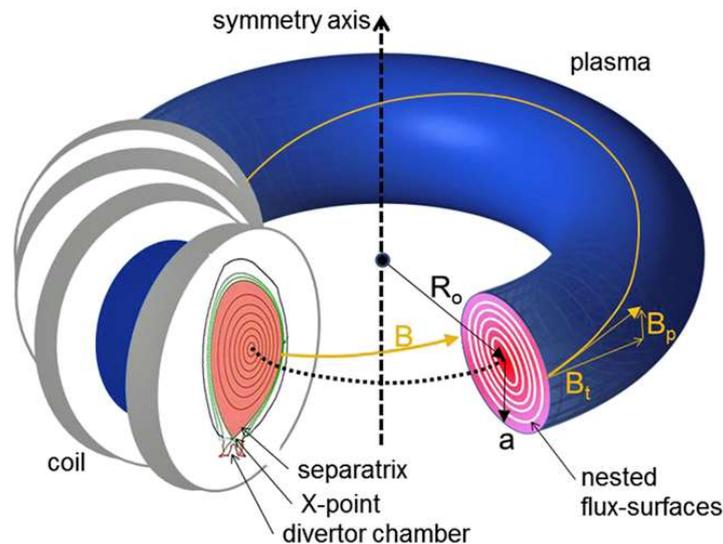
Figure 1.2 - Magnetic field configuration in a tokamak [6]

A tokamak is a complex system[1], but it can be roughly described starting from these basic components and their purposes:

- First wall: the first solid structure in proximity with plasma, resistant to sputtering, thermal loads and mechanical loads, and with a plasma compatible material (W, Be). Magnetic confinement is not a perfect confinement; therefore, the first wall must withstand high thermal and mechanical loads. Being a thin layer increases thermal performance, which is good as Tungsten is not a good thermal conductor.
- Divertors: a specific portion of first wall where plasma particles are forced to collide with. This component withstands the highest energy fluxes, and its cooling functions are enhanced in every possible way. Impurities from divertors have less probability to reach the main plasma because divertors are located further than the first wall from the main plasma.
- Breeding Blanket: the first area in the inner structure beyond the first wall, where Lithium is irradiated by neutrons producing Tritium, then extracted with Tritium Extraction systems such as Permeation Against Vacuum. The blanket can also work as a power extractor and as shield.
- Magnets: superconductive magnets (Toroidal Field coils, Poloidal Field coils, Vertical Field coils) are necessary for plasma confinement and stability. They must be cooled to extremely low temperatures (4 K) to keep superconductive properties and they are extremely sensible to radiation damage, due to radiation heating and damage on the lattice itself. However, High Temperatures Superconductors (HTS) have higher critical temperatures, higher critical current at the same temperature and overall better performances. Research and development on these new technologies, as well as an evaluation of their feasibility, advantages and disadvantages in a fusion reactor are vital for ARC.
- Shields: keep radiation away from magnets and workers.
- Cooling system: Cool down the entire system, extract power.

1.3   ARC: Affordable Robust Compact.

ARC is a project carried by PSFC (Plasma Science and Fusion Center) and MIT (Massachusetts Institute of Technology) to imagine the best fusion reactor's model possible with the available technologies[5], [9]. ARC is different from other tokamaks in many and innovative aspects and its design is constantly improving as technology does. ARC design was carried out thinking about how to decrease economic costs to make a fusion reactor; the answer is a reduction in the complexity and in the size of the reactor (Figure 1.3). This reduction

in size is possible thanks to HTS (High Temperature Superconductors), a new type of superconductors such as REBCO tapes, that can maintain superconductivity properties at higher temperatures and can withstand higher critical currents to produce stronger magnetic field than the average superconductive magnet. This technology is still under research and development, because an increase on superconductor's performance is an enormous advantage for high power density fusion reactors such as ARC. To quantify the importance of magnetic field we can express the power produced by a tokamak as $P \propto V * B^4$, and the cost is directly proportional with the volume. With a great decrease in cost, it is even possible to think of a privately funded fusion reactor. However, as tradeoff, one of the issues from size-decrease is that superconductive magnets are more exposed to radiation damage, therefore shielding must be analyzed and improved if it is necessary. Parameters which characterize ARC, such as the plasma power, the size and the intense magnetic field, are described in Table 1.1.
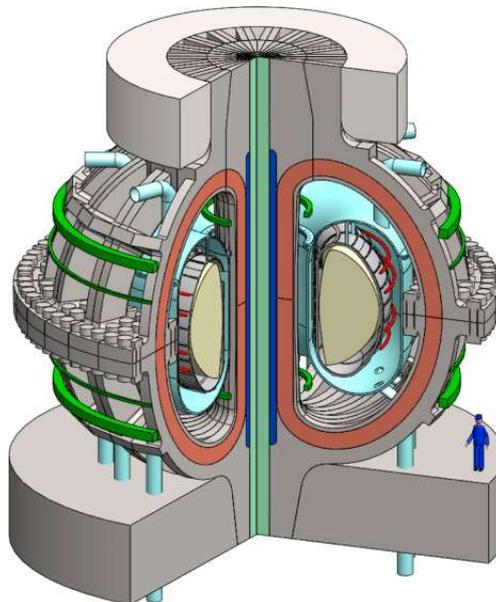
Figure 1.3 - ARC conceptual image for 500 MWth [5]*.*

Table 1.1 - Principal parameters for ARC [10]*.*

Design parameter	Value
Fusion power	525 MW
Total thermal power	708 MW
Total electric power	283 MW
Plant thermal efficiency	0.40
Major radius	3.3 m
Plasma semi-minor radius	1.13 m
Toroidal Magnetic Field	9.2 T
Plasma current	7.8 MA
Tritium breeding ratio	1.1
Energy confinement time	0.64 s

1.3.1   Molten-Salt Blanket

ARC's blanket's design is deeply innovative and unique compared to traditional breeding blankets. The entire structure, vacuum vessel, divertors and plasma chamber, is immersed into the structureless liquid blanket of

molten salt (FLiBe). FLiBe breeding blanket fulfills many important roles at the same time; FLiBe acts excellently as coolant for the vacuum vessel, as Tritium breeder and carrier for Tritium production, and as shield to prevent neutron damage to magnets. Having a liquid breeding blanket fulfilling many critical functions instead of a dedicated system for each one has many benefits, such as the reduction on the complexity of the structure, and therefore a reduction of costs, a space saving in the vacuum vessel, a reduction on structural materials that undergo neutron damage and activation with the decrease of radioactive wastes, and a better management of maintenance, because the reactor can be drained to perform maintenance operations and the vacuum vessel can be completely replaced independently from the breeding blanket. The reduction of structural materials also means a better neutron economy for Tritium production and a reduction on radioactive wastes production.

FLiBe is a molten salt composed of a mixture of LiF and BeF_2 with a ratio of 2:1 (Li_2BeF_4). This mixture is well suited for nuclear fusion application because of its low activation properties, low electrical conductivity (decrease on MHD effects) and Tritium breeding properties. Some issues with Tritium are due to corrosion, high melting temperature (730 K) and high viscosity, but technologies are available to deal with these issues.

FLiBe starts flowing poloidally inside the vacuum vessel, in a channel between the two bi-layered walls that form the vacuum vessel, cooling it as result. This channel is crucial for cooling the vacuum vessel, power extraction and Tritium production, because neutron flux is at its maximum in this region. This aspect is enhanced further by a layer of neutron multiplier. Then FLiBe flows in the tank where the entire structure is immersed (Figure 1.4). FLiBe in this region cools down exterior layer of Vacuum Vessel, shields external components from neutron flux reducing it drastically, extracting more power as it does so. Then, FLiBe outgoing the tank will be processed to Tritium extraction, purification, and heat exchange processes.
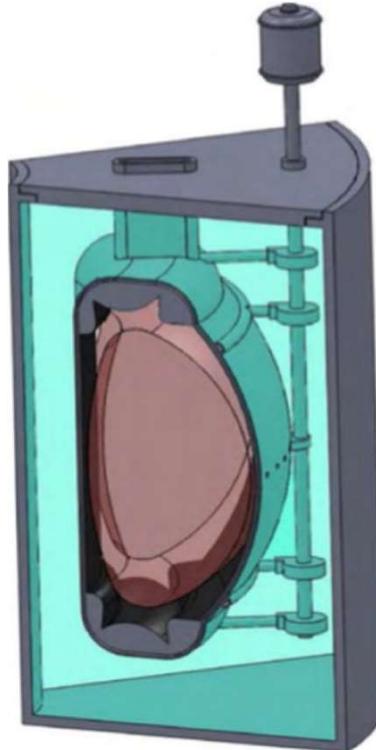

Figure 1.4 – ARC liquid immersion blanket concept [6].

1.3.2 Vacuum Vessel

ARC's vacuum vessel is made with as little structural material possible, to decrease radioactive wastes, decrease costs and to make it replaceable. As ARC's magnets are demountable (Figure 1.5), it is possible to replace the entire vacuum vessel with little downtime and reduced economic cost (the breeding blanket, which is expensive in traditional tokamaks, is not part of the vessel). This characteristic softens the radiation damage and creep damage issue on performance, as the entire vessel can be replaced after its lifetime, yet to determine [9]. If plasma disruption happens, the vessel that incurs the highest damage can be replaced without other expensive components being involved in the accident.
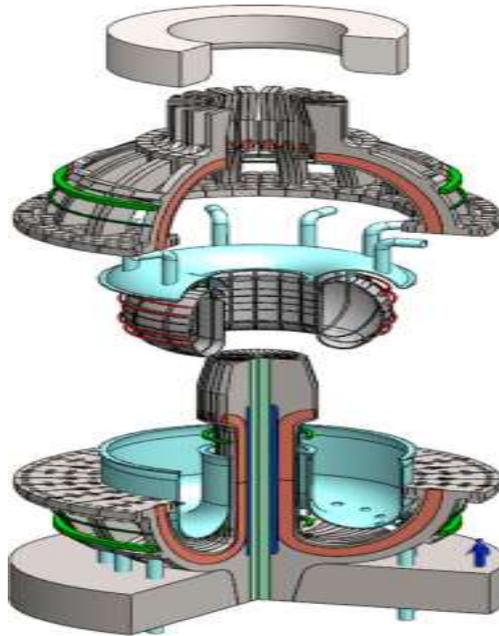

Figure 1.5 - ARC maintenance scheme [2].

The vacuum vessel has 4 layers (Figure 1.6), each one with a dedicated function:

- The first wall, first solid material in direct contact with plasma, is made of Tungsten, a material well suited to withstand high Temperatures and high sputtering loads from plasma, with the disadvantage that impurities in plasma due to sputtering irradiate a lot of power ($P_{irr} \propto Z^2$) with the possibility to turn off the plasma. This layer's thickness is 1 mm.
- Right behind Tungsten's layer, an Inconel 718 layer of 10 mm withstands mechanical loads and provides robustness to Tungsten. Inconel 718 is a Nickel-based alloy with excellent mechanical and thermal properties and high corrosion resistance, but also high neutron activation. This layer is wet by FLiBe channel, providing cooling for first wall and the entire Vacuum Vessel. Other alternatives to replace Inconel 718, such as EUROFER97 and V-15Cr-5T are already considered and they will be tested [11].
- On the other side of FLiBe channel, a Beryllium layer of 10 mm provides neutron multiplication to improve neutron economy and enhance the Tritium production (Tritium Breeding Ratio). Beryllium can also act as a corrosion mitigator due to its interactions with F ions.
- Another 30 mm Inconel 718 layer provides mechanical loads resistance to the entire vacuum vessel. Beyond this layer, FLiBe liquid blanket in which the vacuum vessel is immersed provides ulterior cooling to this layer.
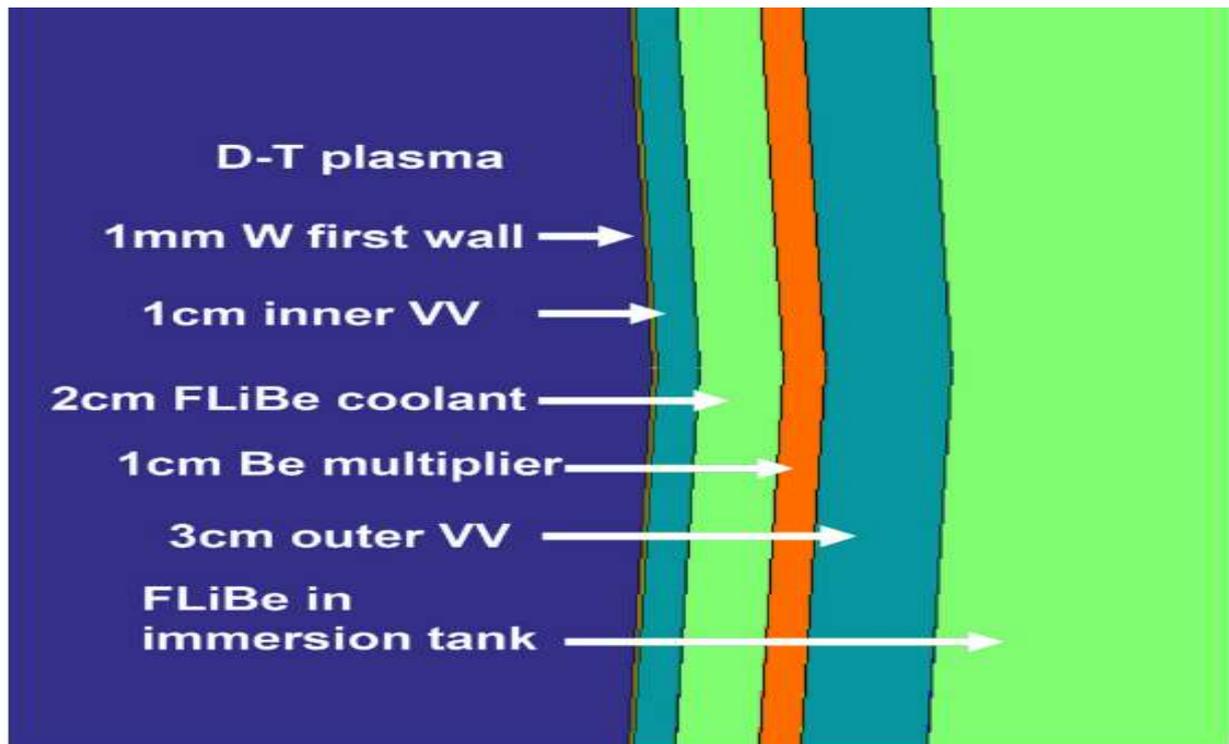
Figure 1.6 - Scheme and materials for vacuum vessel's layers [7].

2   COMSOL CFD model for ARC

COMSOL Multiphysics [12] is a finite element analysis software that can couple different physics for mechanical, electrical, chemical, thermal, acoustic applications and more. Every COMSOL model is composed of 7 sections:

- Component: section where the dimension of the problem is defined (1D,2D, 3D, 1D axisymmetric,2D axisymmetric);
- Definitions: parameters, initial data, variables and function definitions;
- Geometry: COMSOL has a built-in CAD for building the geometry for the model;
- Materials: material properties and domains are defined in this section;
- Physics: analyzed domains, boundary conditions, governing equations to describe the physics of the problem are set here. It is possible to analyze and merge different physics into a multiphysics (e.g. thermomechanical stresses);
- Mesh: mesh assembly and properties are done in this section;
- Study: study settings (stationary, time dependent, eigenvalues…), initial conditions and solvers are set in this section;
- Results: plots, tables and derived values are extracted from the results section;

In the paragraph below each of these steps will be explained for the ARC's reactor thermo-fluid dynamic model.

2.1   Model: Vacuum Vessel and tank

2.1.1   Component

The computational domain chosen for this model is a section of the reactor, because of its toroidal symmetry. Therefore, the result approximates the actual reactor, which cannot be perfectly axisymmetric; however, considering that some geometrical traits of the final model are not decided yet, and the actual model is axisymmetric, this approximation is well justified. In conclusion, a 2D axisymmetric component was chosen for this model.

2.1.2   Geometry

A section of ARC reactor is built using COMSOL built in CAD. The starting point to sketch ARC's geometry is plasma's shape: ARC's plasma has minor radius of 1.13 m, elongation of 1.8 and triangularity of 0.375 [9]. With these parameters it is possible to make a rough sketch of plasma's shape using ellipses and consequently make the first wall according to it (Figure 2.2). Starting from vacuum vessel drawing known quantities (Figure 2.1), and adapting unknown quantities, the final sketch for first wall and vacuum vessel has been done, already with layered walls. Layers thicknesses are described in the Table 2.1.
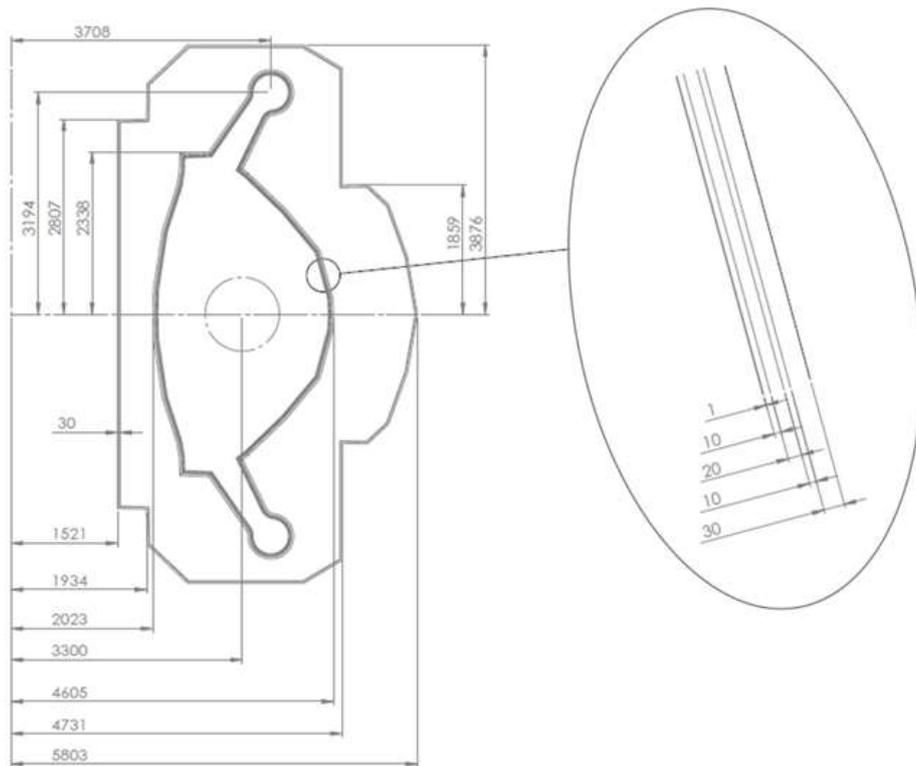
*Figure 2.1 – ARC geometric measures in mm* [13].
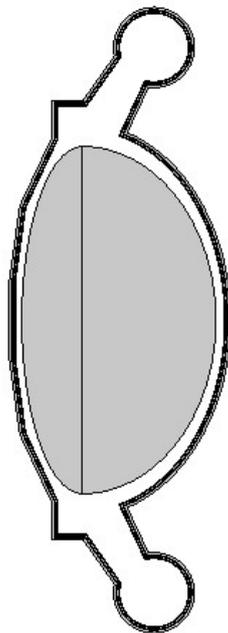
Figure 2.2 - Plasma and vacuum vessel sketch for COMSOL model; grey region is plasma's sketch.

Table 2.1 - Thicknesses of each layer in vacuum vessel.

Material	Thickness [mm]
Tungsten	1
Inconel 718	10
FLiBe	20
Beryllium	10
Inconel 718	30

The geometry construction can be divided into four regions with different characteristics:

- Inner blanket region (toward the axis of the torus) is composed of straight layered segments, with inclination following plasma shape;
- Outer blanket region is made with layered elliptical arc with the same center as plasma's shape center, and a slighter bigger radius;
- Foot region's radius is 0.5 m [9], then adapted to 0.4 m to better fit inside the tank;
- Long legs connecting main plasma with divertor regions have inclination of 55° and 65°.

The entire structure is symmetrical in toroidal direction. Each domain (one for each layer) is continuous and does not overlap with adjacent ones.

Other significant changes in the geometry are made on this sketch to adapt it better to the physics, thinking about the inlet and outlet configurations for FLiBe channel (Figure 2.3):

- One inlet on the shoulder region of the outer blanket, following the elliptical region and outflowing just before the leg region on the bottom;
- one inlet on the leg region on the bottom, flowing across the lower foot region and outflowing after the other lower divertor's leg;
- one inlet on the inner blanket region, just before the upper long leg region, flowing across the breeding blanket and reaching the lower divertor region;
- one inlet on the inner blanket region, at the beginning of the long leg on the upper divertor, covering upper divertor and long leg and outflowing at the end of the leg region in the outer blanket.
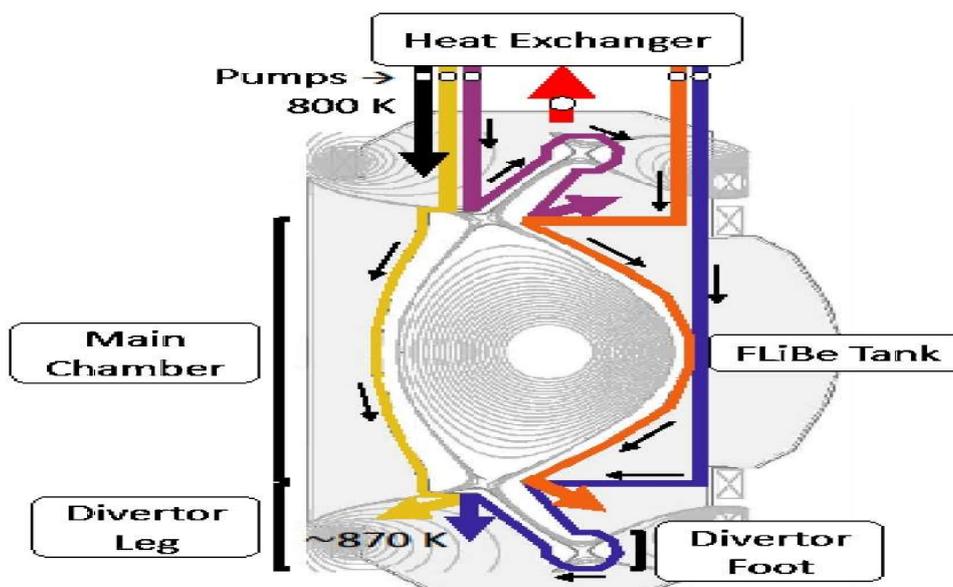
Figure 2.3 - Schematic of the vacuum vessel showing FLiBe flowing in different regions [9].

ARC geometry is divided in different areas named by a letter to identify the area represented in Figures of this work (Figure 2.4):
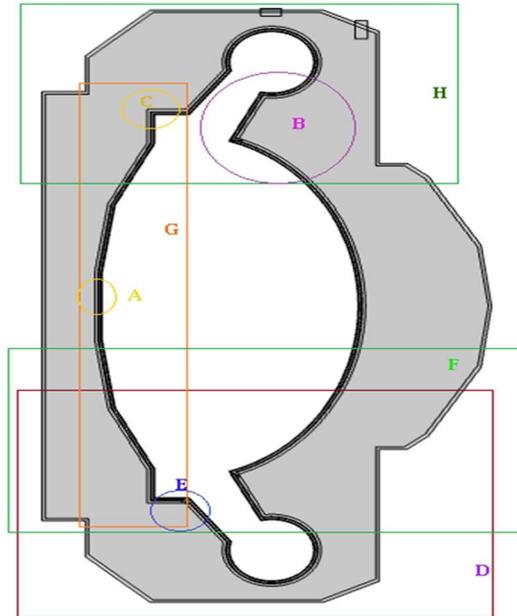
Figure 2.4 - ARC different regions named by letter.

To create the connection between the channel and the tank region, on the Inconel 718 and Beryllium region a channel deviation through vacuum vessel's outer layer was made to make space for FLiBe outflow into the tank. The wall which deviates the flow to this outlet is a prolongation on the inner Inconel 718 structure (Figure 2.5). A small gap in the geometry just before inlets is made to position inlets in those specific positions, because inlet boundaries cannot be internal boundaries.
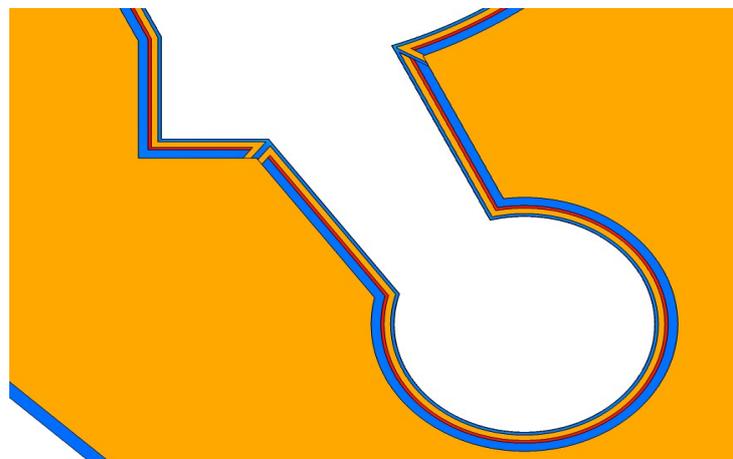
Figure 2.5 - Leg and foot region for ARC. Outlet model from vacuum vessel to tank. FLiBe is orange, Inconel blue, Beryllium red. Tungsten is darker blue, but as 1 mm thin layer it cannot be seen.

Tank's geometry available from the sketch [13] is followed precisely (Figure 2.6). For unknown measures on the rounded corners some sketches were made according to results and data to find the better fitting geometry. The tank itself is a 30 mm single-layered wall made of Inconel 718. An outlet channel and an auxiliary inlet channel [9] were added after making some considerations from preliminary results. Tank and vessel's geometries do not overlap, but they are modelled as complementary domains. Therefore, vessel "outlet" is directly connected to tank "inlet" if the model deploys both geometries.
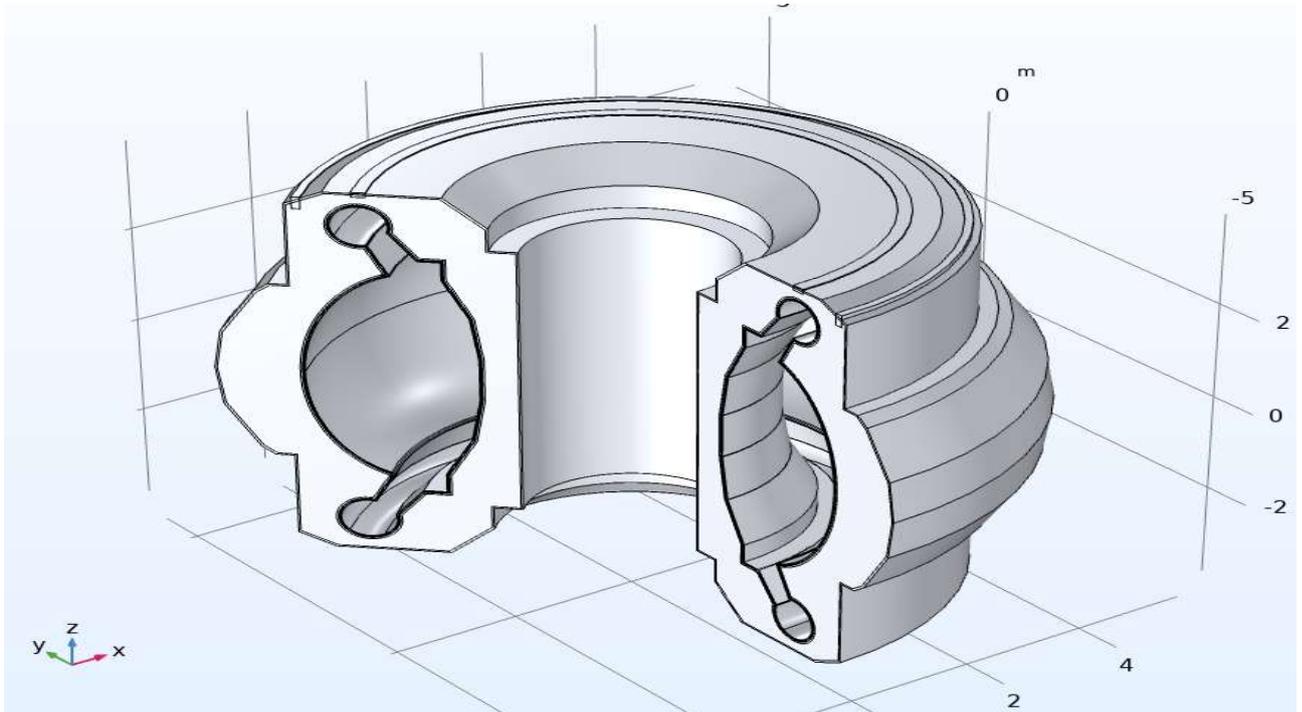
Figure 2.6 - ARC Reactor geometry built in COMSOL Multiphysics.

Exact volumes of each material (Table 2.2) can be used to evaluate the cost of the raw materials for ARC reactor, both for first construction and further replacements. Other applications of these values can be the estimate of the weight of the reactor, the estimate of how much energy is needed to heat the reactor to operational conditions, how much FLiBe is needed in the cooling and Tritium extraction circuit, how much of low-level radioactive wastes are produced.

Vessel's internal surface area is an interesting data to evaluate power coming from plasma irradiation.

Tank's external surface area can be an interesting data to estimate heat losses in a further model that account for them and to evaluate Tritium leakage.

Table 2.2 - ARC volumes and geometrical results.

Geometrical parameters	Values
Tank Volume	353.9 m^3
Tungsten volume	0.4 m^3
Inconel 718 volume	30.8 m^3
Inconel 718 vacuum vessel volume	15.4 m^3
FLiBe volume	319.0 m^3
Beryllium volume	3.8 m^3
Section Area	16.0 m^2

Mean toroidal radius	3.5 m
Plasma surface area	381.2 m^2
Vacuum vessel, external surface area	388.1 m^2
Tank external surface area	458.2 m^2

2.1.3 Materials and Properties

Main material properties used in the COMSOL model and their references are shown in Table 2.3.

<p align="center"><i>Table 2.3 - Material properties in function of temperature.</i></p>

	Inconel 718 [14]
$k\ [W/m \cdot K]$	$3.495867 + 2.673305E - 2 \times T - 1.11803e - 5 \times T^2 + 3.606836E - 9 \times T^3 + 8.235547E - 14 \times T^4$
$\rho\ [kg/m^3]$	8.19
$c_p\ [J/kg \cdot K]$	$361.3373 + 0.2378248 \times T + 7.560689E - 6 \times T^2$

	Tungsten [12]
$k\ [W/m \cdot K]$	$240.51 - 0.2899 \times T + 2.5403E - 4 \times T^2 - 1.0263E - 7 \times T^3 + 1.5238E - 11 \times T^4$
$\rho\ [kg/m^3]$	$19302.7 - 2.3786E - 1 \times T - 2.2448E - 5 \times T^2$
$c_p\ [J/kg \cdot K]$	$116.37 + 7.1119E - 2 \times T - 6.5828E - 5 \times T^2 + 3.2396E - 8 \times T^3 - 5.4523E - 12 \times T^4$

	Beryllium[14] [15]
$k\ [W/m \cdot K]$	$430.35 - 1.1674 \times T + 1.6044E - 3 \times T^2 - 1.0097E - 6 \times T^3 + 2.3642E - 10 \times T^4$
$\rho\ [kg/m^3]$	1848
$c_p\ [J/kg \cdot K]$	$606.91 + 5.3382 \times T - 4.1726E - 3 \times T^2 + 1.2723E - 6 \times T^3$

	FLiBe [16] [13]
$k\ [W/m \cdot K]$	$2413.10646 - 0.4884 \times T$
$\rho\ [kg/m^3]$	1.1
$c_p\ [J/kg \cdot K]$	2386
$\mu\ [Pa \cdot S]$	$1.16E - 4 \times e^{3755/T}$

2.2 CFD physics

To solve the velocity and temperature field of ARC breeding blanket and vacuum vessel the final model must describe non-isothermal single-phase flow for fluid domain, heat transfer equations for solid domain and a model for convective heat transfer to couple both physics.

Starting from a guess of Reynolds number it is possible to estimate if the flow in the channel region will be laminar or turbulent: For an 800 K FLiBe flowing in a 20 mm wide channel at the velocity of 2.7 m/s, $Re = \frac{\rho U L}{\mu} = 8616$, therefore the flow is beyond the laminar-turbulent transition on the turbulent region. Tank's region flow is turbulent as well, determined by an analysis *a posteriori*.

COMSOL has physics for turbulent flow models: for ARC's model, the Realizable k-Ɛ model has been chosen for its improved performance with flows involving strong streamline curvature and recirculating flows. However, k-Ɛ model is used first to determine initial conditions for a better convergence of further models. This model solves the Navier-Stokes Equations [1] for steady state and turbulent k-Ɛ approximation:

$$\rho(\boldsymbol{u} \cdot \nabla)\boldsymbol{u} = \nabla \cdot [-p\boldsymbol{I} + \boldsymbol{K}] + \boldsymbol{F} + \rho \boldsymbol{g}$$

---

[1] As reported in COMSOL.

$$\nabla \cdot (\rho \boldsymbol{u}) = 0$$

Where ρ is the density, $\boldsymbol{u}$ is the velocity vector, p is the pressure, $\boldsymbol{I}$ is the identity matrix, $\boldsymbol{K}$ is the stress tensor, $\boldsymbol{F}$ is the force vector and $\boldsymbol{g}$ is gravity acceleration.

COMSOL has a dedicated multiphysics for solid and fluid heat transfer, the *conjugate heat transfer*, both for laminar and turbulent flows. This model encapsulates heat transfer equations for solids and fluids, turbulent flow model and it simulates convection too, by combining the above-mentioned physics. Heat transfer equation solved for steady state liquid and solids is:

$$\rho c_p \boldsymbol{u} \cdot \nabla T = \nabla(k\nabla T) + \ddot{Q}$$

Where c_p is the specific heat capacity, T is the temperature, k is the thermal conductivity and $\ddot{Q}$ is the power generation density.

2.2.1 Turbulent Flow k-Ɛ

Only FLiBe domains are chosen for this physics. Weakly compressible flow is set, as FLiBe flow unrealistically can reach supersonic velocities. Initial values for velocity field are fluid at rest, because k-Ɛ method is consistent enough to find the solution even with a bad initial guess. More accurate turbulence models will use k-Ɛ results as initial condition for consistent convergence. Initial pressure is set at 2 bar [13]. Gravity is added with a check on gravity model that COMSOL Multiphysics has done to automatically include gravity acceleration in turbulent models, including buoyancy and buoyancy-induced turbulence.

Each boundary is set as wall, those which are not, are overridden by their corresponding boundary condition, such as inlets and outlets. Walls include Beryllium-FLiBe and Inconel-FLiBe interfaces in the vacuum vessel's channel, tank's FLiBe and external vessel's Inconel 718 boundaries, tank's FLiBe and Tank's Inconel 718 outer shell boundaries. Inlets are set as described in the geometry section (Section 2.1.2); this was possible thanks to the 1 mm gaps made in FLiBe domain right before the inlet, because, in COMSOL, internal boundaries cannot be inlets. A supplementary inlet beside the tank's outlet is set. The tank's outlet and supplementary inlet are on the upper edge of the tank, being the inlet the most external channel. Inlets boundary conditions are set to fully developed flow, to have an inlet profile describing an already developed flow. Inlet velocities are set according to results and the constraint for velocity-enhanced corrosion. Outlet's pressure boundary condition is set at 3 bar, defining the entire system's pressure.

2.2.2 Heat transfer in solids and fluids

This physic model must be applied to the entire domain. Then Solid and Fluid domain must be specified; Beryllium, Tungsten and Inconel 718 domains are set as solid and FLiBe's domain is set as liquid. Solid-liquid interface's convective heat transfer is handled by the model without further actions. The same applies for Solid-Solid interfaces' conduction as well. This physics was chosen because it estimates the convective heat transfer coefficient without knowledge a priori of it.

Tungsten-plasma interface is modelled with the "Heat Flux" boundary. Material selected is set as Solid, and the heat flux as *General inward Heat Flux*, with the constant value of 0.5 MW/m^2. A better Plasma heat flux distribution is possible both by implementing a function instead of a constant value, or by setting different constant values for different region's boundaries. However, data is still lacking on plasma's heat flux distribution, therefore a constant average value is a necessary approximation.

Input Data Power Generation

Volumetric heat generation is modelled by the *Heat Source* interface, each layer with its own interface. FLiBe's material is set to *Nonsolid*, while Inconel 718, Tungsten and Beryllium as *Solid*. Then a *General Source* [MW/m^3] was set for each material as described in Table 2.4 as first guess.

Table 2.4 - Power distribution in ARC blanket [9]*.*

Material	Volumetric power generation $[MW/m^3]$
Tungsten	24.1
Inconel 718, inner layer	11.3
FLiBe, channel	11
Beryllium	6.3
Inconel 718, outer layer	7.4
FLiBe, tank	1.1
Inconel 718, tank	0.04

In a subsequent model a more precise power generation profile was implemented: starting from volumetric power generation data from neutronic models, as reported in [13] and done with OpenMC [17], adapting the idealized reactor data to the COMSOL one, an exponential power density distribution depending on the distance from the first wall was implemented as described in Table 2.5.

Table 2.5 - New power distribution evaluated.

Material	Volumetric power generation $[MW/m^3]$
Tungsten	21.7
Inconel 718, inner layer	10.1
FLiBe, channel	9.64
Beryllium	5.58
Inconel 718, outer layer	6.56
FLiBe, tank, average value	0.8
Inconel 718, tank	0.04

In Figure 2.7, the volumetric power generation in the tank, starting from the interface of vessel external layer, is shown according to neutronic models results. The neutronic model presented evaluated the neutronic flux, and consequently power generation, for the distance of the nearest magnet. There are tank region further than the last evaluated point, but it the gradient of this negative exponential distribution is smaller in this areas and power generation too, therefore as a conservative approximation the power generation after 0.6 m is considered constant.
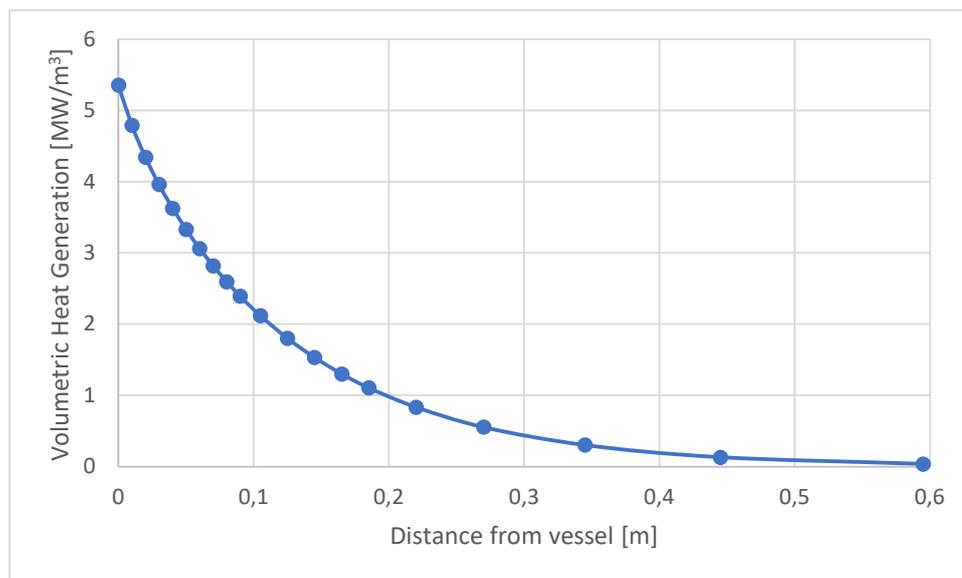

Figure 2.7 - Power generation distribution

This improvement on the power generation's distribution has a noticeable impact on the precision of the results, especially in tank's peripheric regions. Although Table 2.5 values seem lower than the first guess, these values are a direct result of a neutronic simulation, and have a better fit for ARC simulation because of different volumes and geometry measures from the article [9].

Inlet temperature conditions for FLiBe are set to 800 K and outlet boundary is specified in concordance to the fluid-dynamic model. The rest of the boundaries are set to adiabatic to make a conservative guess (tank's shell external boundary, fictitious boundaries next to inlets).

Multiphysics bonds the variables of both the models to compute a non-isothermal turbulent flow.

2.3 Mesh Generation and Grid Convergence Index

COMSOL has a built-in physics-controlled mesher. This function is useful for fast reaching the results; however, a custom-built mesh has many advantages because there is much more control over each aspect.

The geometry is divided into different domains due to their characteristics; unstructured triangular mesh is used for each of them, but further options and size considerations are different:

- Tungsten layer is so thin that it needs a highly refined mesh, being one of the major computational burdens of the model. For quick results, a Tungsten-free model (with plasma heat flux directly on Inconel boundaries) can be used as Tungsten layer has no big impact on other domains;
- Inner Inconel 718 layer needs a refined mesh to transition from the small mesh size from Tungsten to a normal mesh size. A big growth rate and a big difference from smallest and biggest element characterize this layer;
- FLiBe channel domain inside the vessel needs thin boundary-layers to function. Due to the change of directions in the channel, corner refinement to keep boundary layer's quality acceptable is selected for problematic corners;
- Large solid layers such as Inconel 718 and Beryllium layers do not need a fine mesh as fluid domains do;
- Tank's fluid need boundary layers next to the wall regions (blanket and external wall). The whole region's mesh is highly refined because in such a complex geometry it is impossible to foretell where recirculation happens, and the results need to be precise in recirculation regions, as they are fundamental for further models.

Final mesh results are shown in Figure 2.8, while mesh details are shown from Figure 2.9 to Figure 2.12, with indicated in the caption the enlargement area from Figure 2.4.
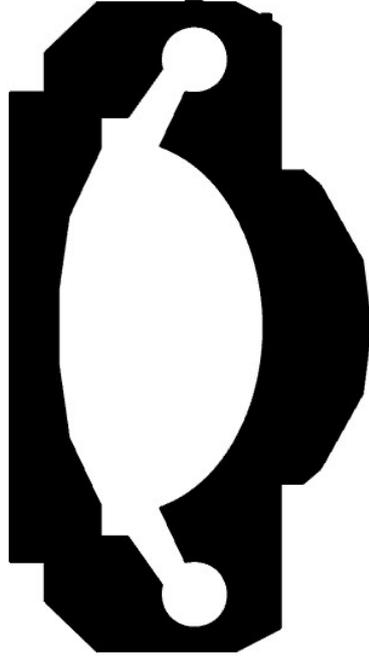
*Figure 2.8 - ARC mesh after mesh convergence study.*
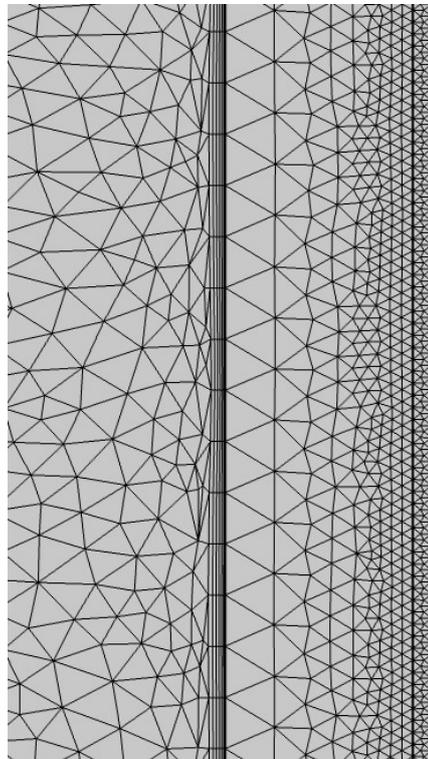
Figure 2.9 - Mesh detail of the transition from Tungsten layer's fine mesh to FLiBe channel mesh thanks to Beryllium mesh [Area A].
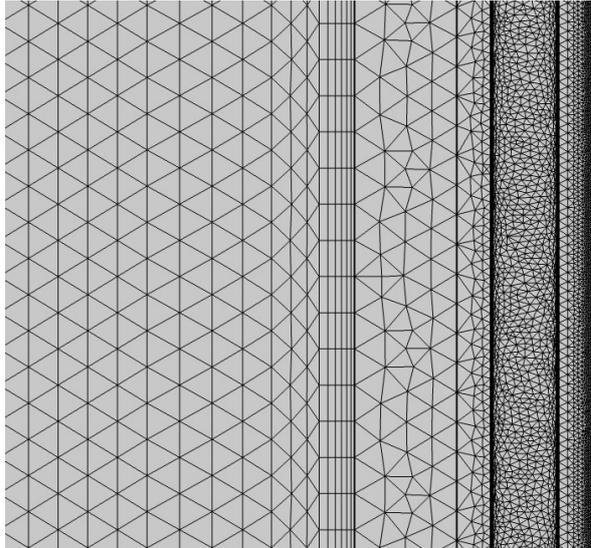
*Figure 2.10 - Mesh from each layer and Tank [Area A].*
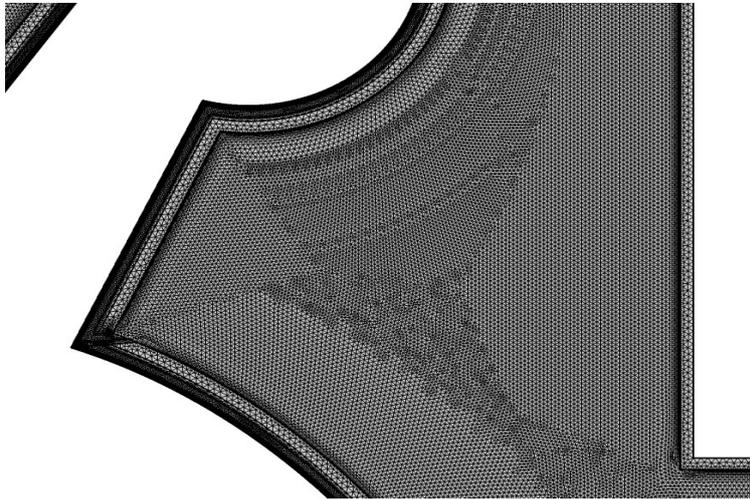

Figure 2.11- Tank's mesh [Area B].
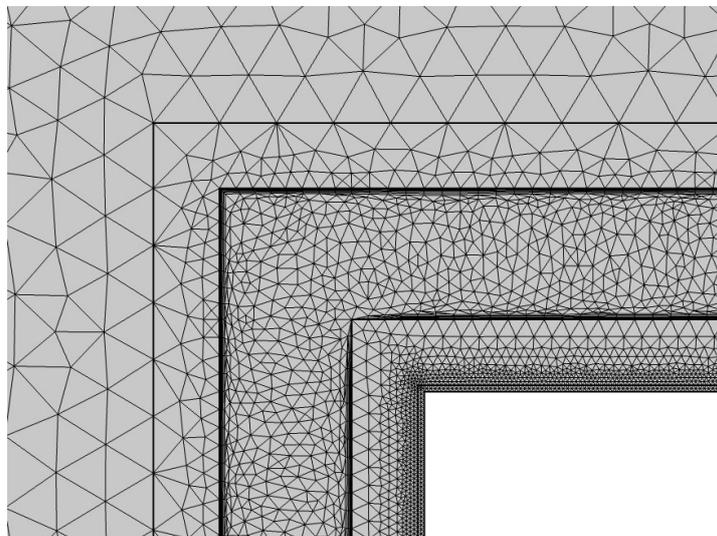
Figure 2.12- Corner refinement [Area C].

Building a correct mesh is fundamental to have reliable results. However, there is a tradeoff between accuracy of results and computational cost. Therefore, it is fundamental to find the optimal mesh to achieve results with low errors and light simulations. The accuracy of results is verified by a grid-convergence study using the Richardson Extrapolation. The Richardson Extrapolation is a grid convergence method first used by Richardson in 1910 [18]. This method can make an estimate on the error of the solution, which may be a good indicator of the mesh quality. Based on that estimate, the optimal mesh size can be evaluated and obtain by refining or coarsening previous meshes.

Although it is known as h^2 extrapolation, as it is born as second-order method, this extrapolation can be employed for the order of accuracy of the algorithm p, which is not necessarily equal to 2. Richardson Extrapolation is based on Taylor expansion starting from the p-th power of h:

$$\varepsilon_h = f_h - \tilde{f} = g_p h^p + g_{p+1} h^{p+1} + g_{p+2} h^{p+2} + \cdots$$

Some assumptions must be made to reliably use Richardson Extrapolation [19]:

- The result must be in asymptotic range for the coarse mesh.
- Systematic mesh refinement, which means that subsequent meshes must scale with the same constant factor r, and no local refinement should be made.
- Smooth solutions: Richardson Extrapolation takes advantage of Taylor expansion and derivatives; a discontinuity or a singularity would reduce the observed order of accuracy to 1 regardless of the formal order of accuracy of the solution.
- Other numerical error sources must be at least two order of magnitude smaller than the discretization error of the finest mesh; otherwise, Richardson Extrapolation will tend to amplify the "noise" giving mixed results.

It is also possible to estimate the order of accuracy of the results "a posteriori", starting from no other information than the results of 3 different meshes: the coarsest mesh h_3, the middle mesh h_2, with ratio $r_{2,3} = \frac{h_3}{h_2}$, and the finest mesh h_1 with ratio $r_{1,2} = \frac{h_2}{h_1}$ ($r_{2,3}$ and $r_{1,2}$ not necessary equal). With the solution for the ith mesh being f_i and $\varepsilon_{i,i+1} = f_{i+1} - f_i$, we can extract the observed order of the solution by solving this equation[18]:

$$\frac{\varepsilon_{2,3}}{r_{2,3}^p - 1} = r_{1,2}^p \left[\frac{\varepsilon_{1,2}}{r_{1,2}^p - 1} \right]$$

As the equation is transcendental in p, it is possible to find the solution using the Newton method, but the author suggests the following iteration method [18]:

$$p = \omega \rho + (1 - \omega) \frac{\ln(\beta)}{\ln(r_{1,2})}$$

$$\beta = \frac{(r_{1,2}^p - 1)\varepsilon_{2,3}}{(r_{2,3}^p - 1)\varepsilon_{1,2}}$$

With $\omega = 0.5$ being a relaxation factor and ρ equal to the previous iteration of p.

When the observed order of accuracy has been determined, we can evaluate the Grid Convergence Index (GCI): the GCI was introduced to have an error indicator that takes into account the refinement factor r and the order of accuracy p in the error's estimation, preventing the misinterpretation of the error by using only relative difference of results. For two different meshes the GCI is evaluated as it follows:

$$GCI_1^{fine} = F_s \left| \frac{\varepsilon_{1,2}}{1 - r^p} \right|$$

$$GCI_2^{coarse} = F_s \left| \frac{r \, \varepsilon_{1,2}}{1 - r^p} \right|$$

Being F_s a safety factor which value can vary from 1 to 3 in relation to the results obtained. For a three-grid study a safety factor of 1.25 can be safely employed [18].

A percentual version of GCI can be evaluated by using a percentual error instead of an absolute error:

$$GCI_1^{fine} = F_s \left| \frac{\varepsilon_{\%1,2}}{1 - r^p} \right|$$

$$GCI_2^{coarse} = F_s \left| \frac{r \, \varepsilon_{\%1,2}}{1 - r^p} \right|$$

$$\varepsilon_{\%1,2} = \frac{f_1 - f_2}{f_1}$$

In this work, a relative error below 5% will be assumed as a good indicator for mesh convergence and reliability of results.

2.4   Study

To solve the non-isothermal turbulent flow at steady state, 3 study steps have been employed, each one with stationary conditions:

First step: only k-Ɛ model is used. This step solves isothermal flow for ARC's complex geometry, making convergence of further steps easier. For this step, a FGMRES segregated solver was used, number of intermediate iterations increased to reach convergence.

Second step: k-Ɛ model, heat transfer in solid and fluids, non-isothermal flow 1, which employs the k-Ɛ model, unlike non-isothermal flow 2 employs the Realizable k-Ɛ model. This step takes the solution from step 1, and it solves temperature distribution both on fluids and solids. The flow pattern does not seem to change drastically due to temperature dependence. Direct solver PARDISO was used to reach convergence.

Third step: Realizable k-Ɛ model, heat transfer in solid and fluids, non-isothermal flow 2. This step takes step 2 as initial condition for further refinement on the solution. As previous models suppressed these physics (Realizable k-Ɛ, multiphysic 2, combination of realizable k-Ɛ and conjugated heat transfer), this step disables previous fluid models, as every model is solving the same variable, creating a conflict between them. Direct solver PARDISO was used to reach convergence.

3   CFD Simulation Results

In this section results for CFD model are shown and analyzed. In the first paragraph mesh convergence results and verification of the model are analyzed. Velocity field in vessel channel and tank region are displayed in the second paragraph, to have a better understanding of the connections with the temperature field results shown in the third paragraph.

3.1   Mesh convergence analysis

The grid convergence method was applied on different meshes (Appendix A). Results are concerning 3 meshes with size and ratios as described in Table 3.1. Mesh convergence method was applied on average temperature, pressure drop and velocity in different blanket areas (Figure 3.1); as mesh results may not be monotonic, oscillations and imaginary part of the order p are neglected. Only the average temperature in FLiBe channel had a bad convergence, with p=-2. Another mesh convergence study with $H_0=0.0033$ has been carried, with a bad convergence still. Therefore, a mesh convergence study focused on the channel region has been carried, because a refinement on the entire mesh was impossible to carry due to computational limits. Channel mesh convergence (Table 3.2) has shown very good convergence on average and maximum temperature, while average velocity results are unreliable (p=-5) and maximum velocity relative error of 8,1% for the coarse mesh and 7,1 % for the finer one. Further mesh refinements are impossible due to computational limits. The chosen mesh for further simulation is the coarsest of the mesh convergence study from Table 3.2, which is finer than the channel mesh in the previous study (Table 3.1). Data and results Tables are shown in Appendix B.

From the results, the intermediate mesh has a relative error less than 2% and will be employed. Average element quality is 0.8279 while minimum element quality is 0.065. Data Tables for this result are in Appendix A. It should be reminded that average velocity results are unreliable for the mesh convergence study, as they are not yet at convergence. Moreover, maximum velocity results in channel region have a relative error of 8%, but further refinement would decrease the error at 7% with great computational cost.

Table 3.1- Mesh properties for ARC grid convergence.

Channel	Base size	Cells Number		
H_3	0.009038	549996	Ratio	
H_2	0.006363	966968	r23	1.420373
H_1	0.004623	1523405	r12	1.376426
Tank	**Base size**	**Cells Number**		
H_3	0.014984	549996	Ratio	
H_2	0.010667	966968	r23	1.420373
H_1	0.007562	1523405	r12	1.376426

Table 3.2 - Mesh properties for channel grid convergence

| Channel	Base size	Cells Number		
H_3	0.0021082	1443037	Ratio	
H_2	0.0017273	1699538	r23	1.220554
H_1	0.0010863	3002690	r12	1.590031
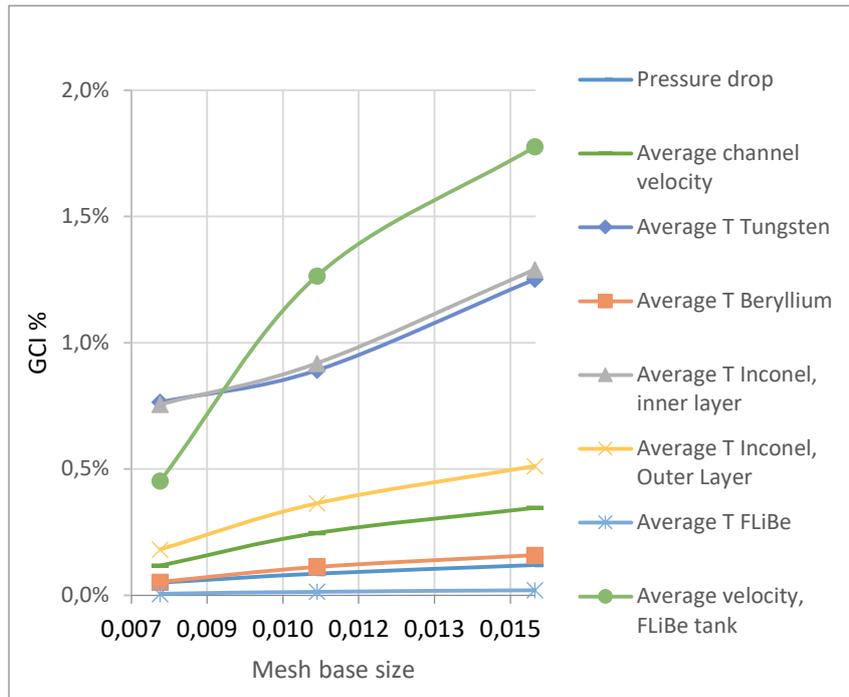
Figure 3.1 - GCI % results, from finest mesh (lower base size) to coarsest.

3.2 Velocity Field Results

In this paragraph FLiBe velocity field in vacuum vessel channel, followed by tank region velocity field, are analyzed.

3.2.1 Velocity field in Vacuum Vessel channel

The first phenomenon observable in vacuum vessel's channel is the influence of the distance from the toroidal symmetry axis on the flow field. This phenomenon is accentuated in divertor channels such as the lower divertor channel (Figure 3.2), where FLiBe accelerates as it approaches the axis (located at x=0); the mass flowrate is constant in the channel, therefore, the acceleration is a direct consequence of the gradual reduction on the flow section. The flow section indeed can be approximated by a circular crown of constant thickness, but with different radius (the distance from toroidal axis), and with an area dependent on this parameter. This phenomenon, coupled with a velocity threshold of 2.7 m/s, affects the flow field for the entire vacuum vessel. Each channel portion must be treated individually due to different geometries, and inlet conditions must be chosen watching closely that the bulk velocity in the smallest section respects the limit. Peripheric regions, therefore with a greater flow section, will experience lower velocities even when the limit threshold is almost reached in the critical points. The more the ratio between maximum and minimum distance from the axis, the more this effect can be observed: the proposed [9] inlet distribution helps greatly to mitigate this phenomenon by dividing the vacuum vessel's blanket in four region with similar distances from the toroidal symmetry axis. Letters at the end of the caption indicates the area enlarged from Figure 2.4.
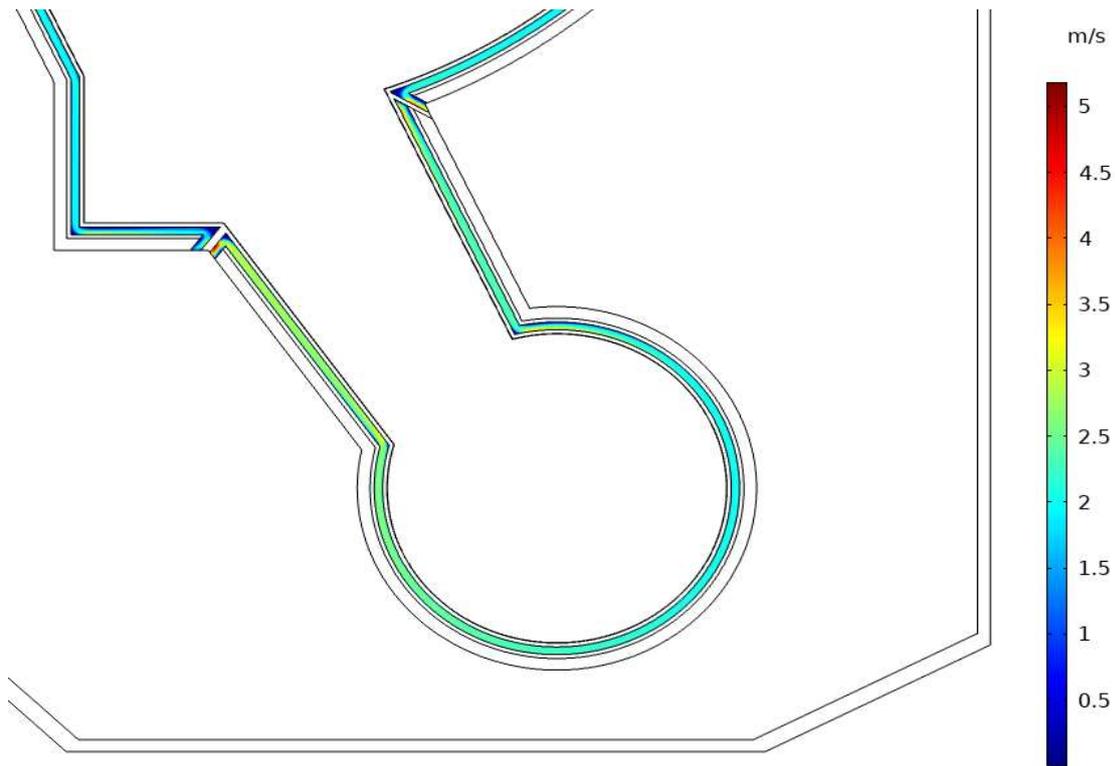
Figure 3.2 - Velocity magnitude in lower divertor channel [Area D].

FLiBe flow in the vacuum vessel channel changes direction on many occasions due to the complexity of the geometry. Consequently, there are unperturbed regions, where the velocity profile is typical of turbulent flows, such as in Figure 3.3, and perturbed regions downstream sharp turns. Because of k-Ɛ wall treatment's boundary conditions, it is expected that the no-slip condition is not respected in velocity profile graphs.
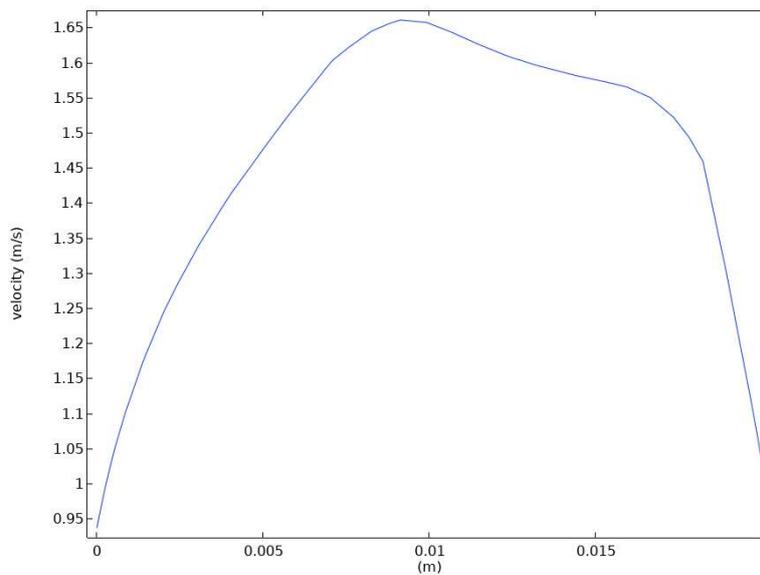

Figure 3.3 - Velocity profile in unperturbed channel region.

FLiBe accelerates after direction changes, as it is possible to observe denser streamlines in the vena contracta (Figure 3.4, Figure 3.5). This increased velocity can represent an issue due to velocity enhanced corrosion effects, therefore turning points must be closely observed. Heat transfer is lightly affected by this phenomenon: corners where velocity is low have a worsened cooling effect, while the accelerated side of the channel should have increased convective heat transfer. The flow field will stabilize into unperturbed condition after 30 cm. The *vena contracta* in Figure 3.5 can be easily seen as it is accentuated due to a sharper turn; there are some recirculating streamlines as well.

Velocity in the lower channel reaches one of the blanket's maximums: the outlet for the lower divertor FLiBe channel is the closest point of the segment to the symmetry axis, therefore FLiBe in the outlet flows across the smallest section, increasing the average velocity. Moreover, the sharp turnaround increases the local velocity in an already critical spot, that must be monitored with increased attention. The criticality of this specific spot is evident if compared to the velocity field in the adjacent channel in Figure 3.5.
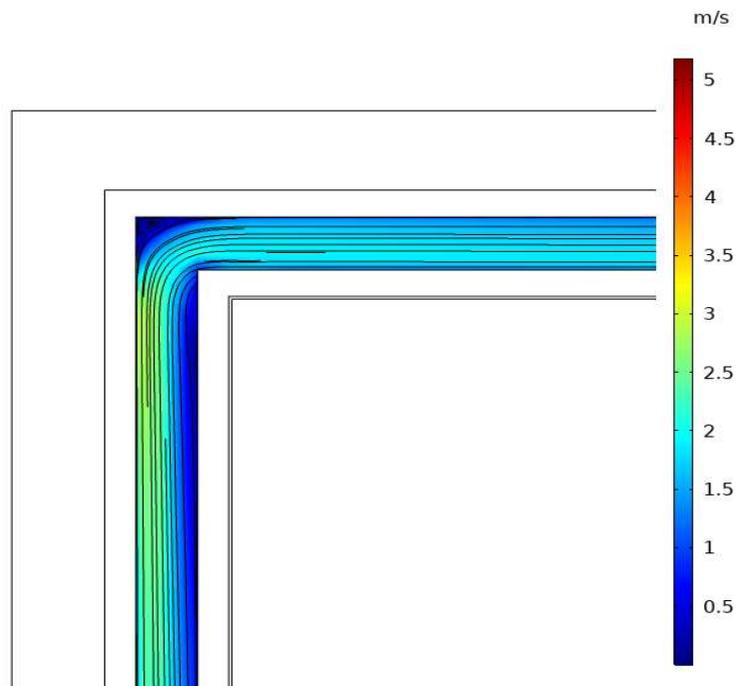

Figure 3.4- Velocity magnitude and streamlines in vacuum vessel's channel: turn detail [Area C].
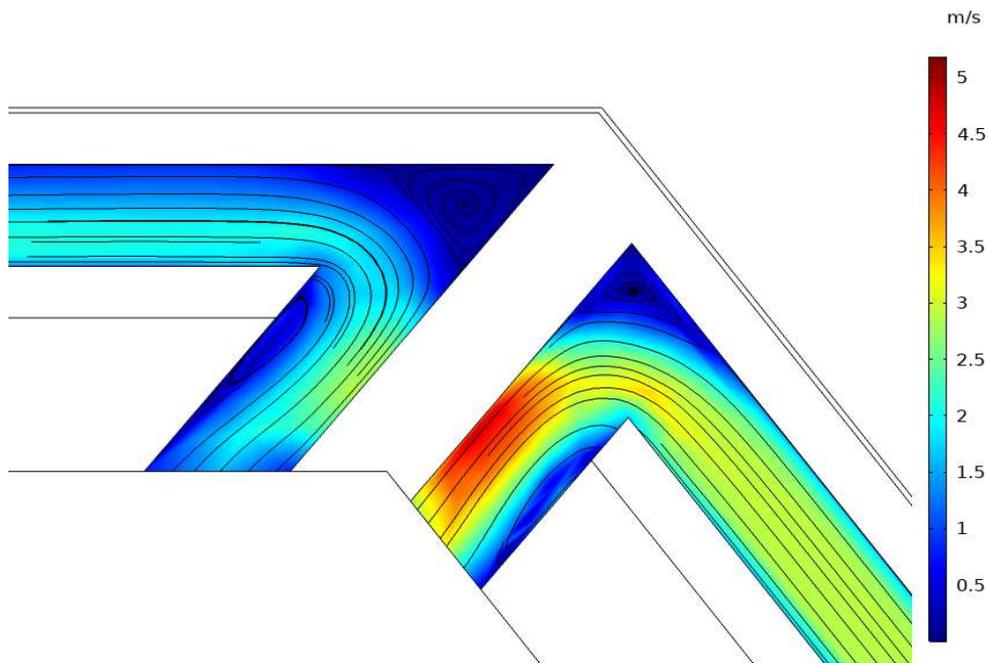
Figure 3.5- Velocity magnitude and streamlines in vessel channel: critical point detail in lower divertor channel's outlet [Area E].

3.2.2   Velocity fields in Tank region

In ARC tank FLiBe flows in a clockwise direction, starting in tank auxiliary inlet and flowing through the whole tank towards the tank outlet. Each mass flowrate coming from the vacuum vessel channels joins this stream. There are some recirculating flows towards some of the corners that this geometry offers. These recirculating regions can have an impact on temperature distribution and may create hotspots where creep limit is not respected, or cold spots where FLiBe solidifies. The location of these recirculating flows, together with the velocity distribution on ARC reactor, is an important result to understand the phenomena involved and to observe, quantify and analyze a result that cannot be easily foreseen without simulations due to the complexity of the geometry and phenomena involved. Results, which are displayed in Figure 3.6, have a bigger impact on temperature and concentration distribution on ARC's reactor. One of the most critical points may be the biggest recirculating flow that takes place in the y=0 axis towards the external peripheral region. Further analysis will be made in Section 4.2.
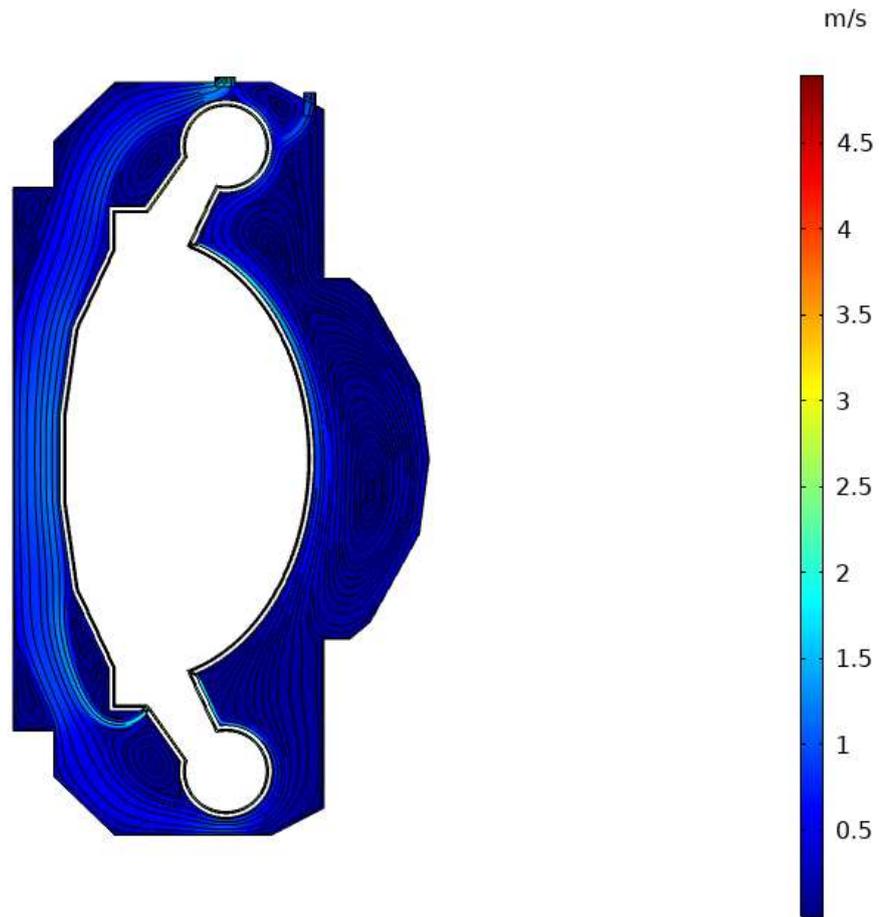
Figure 3.6 - Velocity magnitude and streamlines in ARC's tank.

FLiBe flow field in tank region is dictated mainly on vessel geometry and on the location of connections between channel and bulk tank regions. Therefore, there is a big interest on observing how FLiBe behaves in these connections. On the right of Figure 3.7 it is possible to observe the outlet from the central region channel distant from the axis. The flowrate, as it reaches the tank, goes downwards, joining the overall trend in the tank region, instead of floating upwards, despite FLiBe flowing outside the channel has a lower density than bulk FLiBe in that region, because it is hotter as observed in Section 4.3. On the left side there is the only region in this ARC's configuration where two outlets from vacuum vessel's channel are one next to the other. The lower divertor channel has a bigger flowrate, as its minimum distance from the symmetry axis is bigger than the central channel near the axis. The two flows merge into one which will later join the overall trend in tank's region, however temperature distribution as shown in Figure 3.14 of Section 3.3 can highlight a separation between the two flows that is invisible from this plot.

As three out of four contributions from vacuum vessel to tank flow are in the lower divertor region, FLiBe velocity increases slightly after flowing through it. However, in the same region, three recirculating flows take place: one towards the lower long leg, another one on a corner towards the peripheric shell and a third one above the flowrates coming from the channel (Figure 3.8). Because of their presence, these three regions may be experience critical temperature and concentration distributions, which will be observed in Section 3.2 and Chapter 5.
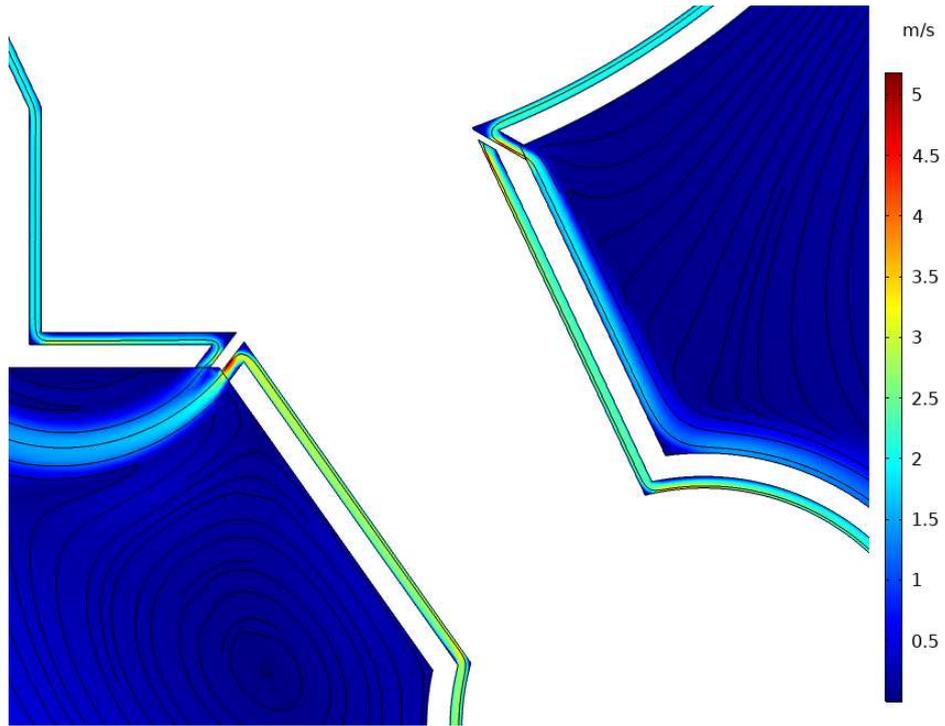
Figure 3.7 - Velocity magnitude and streamlines in ARC: channel-tank connection [Area F].

Figure 3.8 - Flow field in lower tank region [Area D].

3.3 Temperature Field

The temperature field results need to be compared with previous results from the turbulent flow section; temperature fields are tightly connected with velocity fields in this simulation; therefore, streamlines are included in temperature plots to have a better understanding involved phenomena.

3.3.1 Temperature field in Vacuum vessel channel

As FLiBe flows through the vacuum vessel channel cooling down the solid structure, it heats up. It is also evident that FLiBe temperature near walls is higher because solid layers are the material that needs cooling. Layers near the plasma experience the highest temperature in the vacuum vessel, therefore FLiBe temperature gradient near the Inconel wall is harsher compared to the gradient near Beryllium (Figure 3.9).
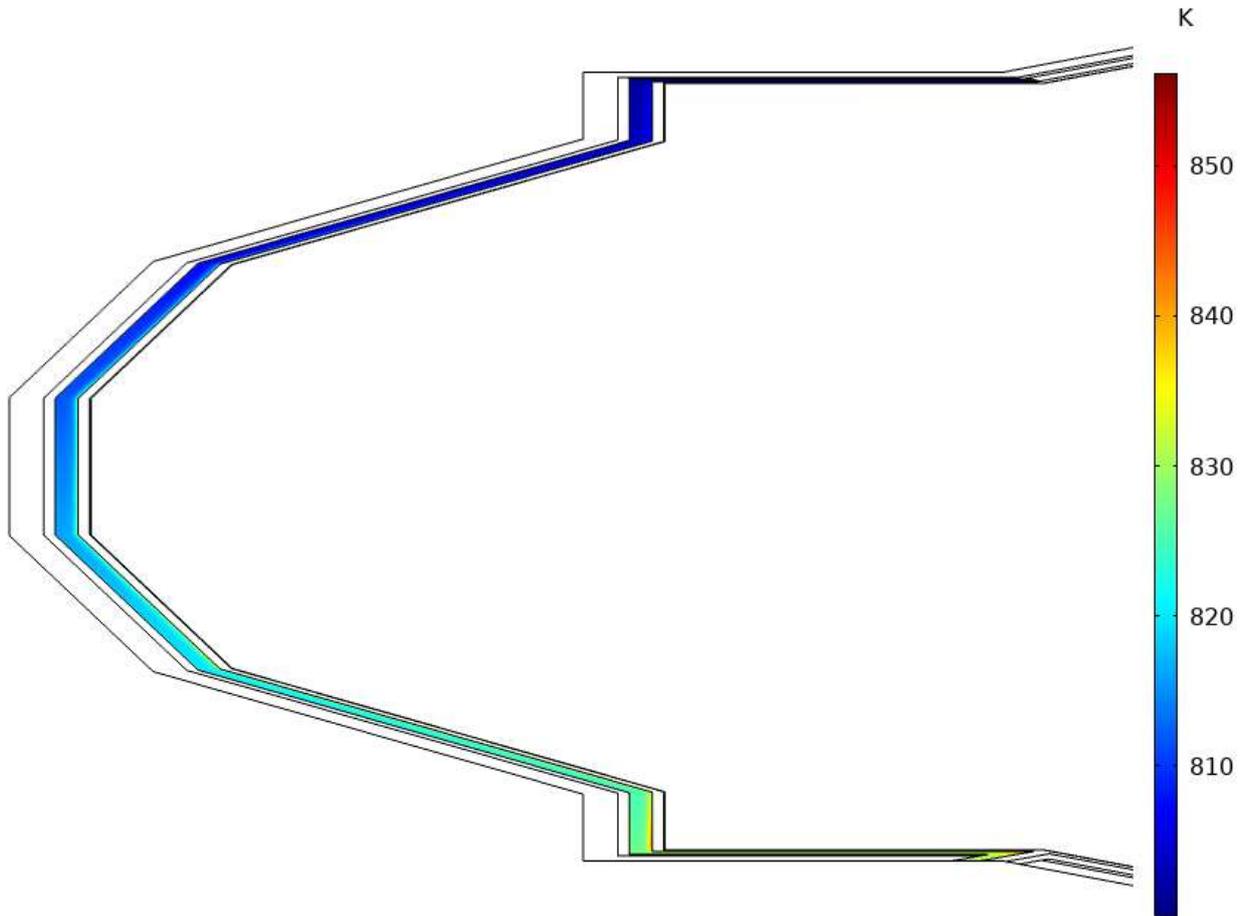
*Figure 3.9 - Temperature increase in vacuum vessel channel (image not in proportion) [Area G].*

The central parts of the vessel experience hotter FLiBe flow near to the end compared to divertor sections, because they are longer (Figure 3.10). Although the innermost central channel has lower flowrate than the external one, it has also a smaller surface and volume irradiated by plasma heat flux and FLiBe heat

generation; in conclusion, results show comparable outlet temperatures for both sides (Figure 3.10). In divertor regions we can observe shorter channels, and in conclusion colder outlets.
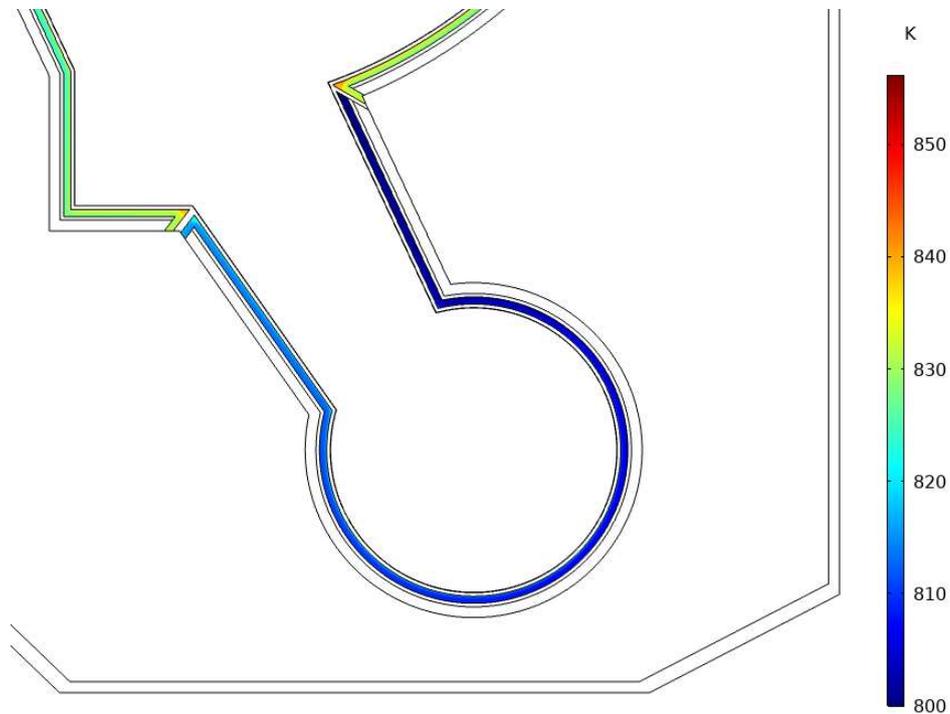

Figure 3.10 - Comparison between divertor and central channels [Area D].

3.3.2   Temperature field in Tank region

In this model tank's convective heat flux is tightly connected with vacuum vessel's external layers temperature. Therefore, an overview on tank's temperature field is necessary before observing vacuum vessel's external layers.

As explained in Section 4.2 FLiBe in the tank flows in clockwise direction; due to power generation in tank and contribution of hot flowrates coming from the vacuum vessel, FLiBe reaches the tank outlet at a temperature of 830 K approximatively. However, outlet temperature is not the maximum FLiBe temperature as there are some hotspots due to recirculating flows. Hotspots are in recirculation regions near the vacuum vessel, where power generation is still high. There are as well other recirculating flows with relatively low temperatures, because volumetric heat generation caused by neutrons is negligible in those areas (Figure 3.11); one of these regions with low temperature is the biggest recirculation in the center, which could have been a critical point for overheat due to its size. In fact, in previous models where power generation was approximated as constant, these regions, especially the biggest, were significantly hotter. Hotspots will have an impact on outer vessel temperatures and criticalities may arise due to them.
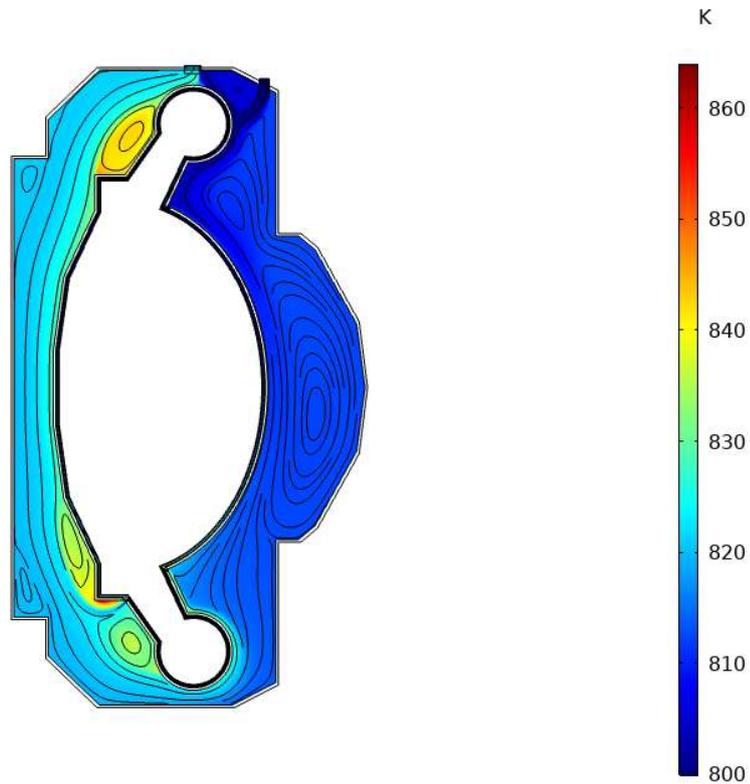
Figure 3.11 - ARC FLiBe Temperature distribution.

In the tank there is a vertical division in two halves, where the external part of the reactor is colder while the internal one is 20 K hotter approximatively (Figure 3.11). This happens because in the auxiliary inlet the temperature is 800 K, the upper divertor channel joins the tanks region but with low temperatures to heat up the FLiBe. A significant income from channel happens before the lower divertor long leg on the external side, heating the bulk FLiBe, and after the lower divertor's long leg on the internal side where two outlets from the channel region are located. So, contributions from channel FLiBe are located all in the lower divertor region, and as a result tank's bulk FLiBe is divided in a "before channels' contributions" and an "after channels' contributions" area.

Temperature distribution in external layers is heavily influenced by FLiBe temperature, due to convective heat transfer. High temperatures in Inconel and Beryllium are observed where FLiBe temperature rises towards the end of the channel, for example the external channel for central region in Figure 3.12. But there are some exceptions: in the lower divertor region, before the long leg section on the outlet side, temperature rises overcoming temperatures near the channel's outlet; the same happens before the outlet in the central channel near the axis, towards a corner. This happens because of some hotspots in tank's FLiBe that have a direct effect on convective cooling of external layers of vacuum vessel.
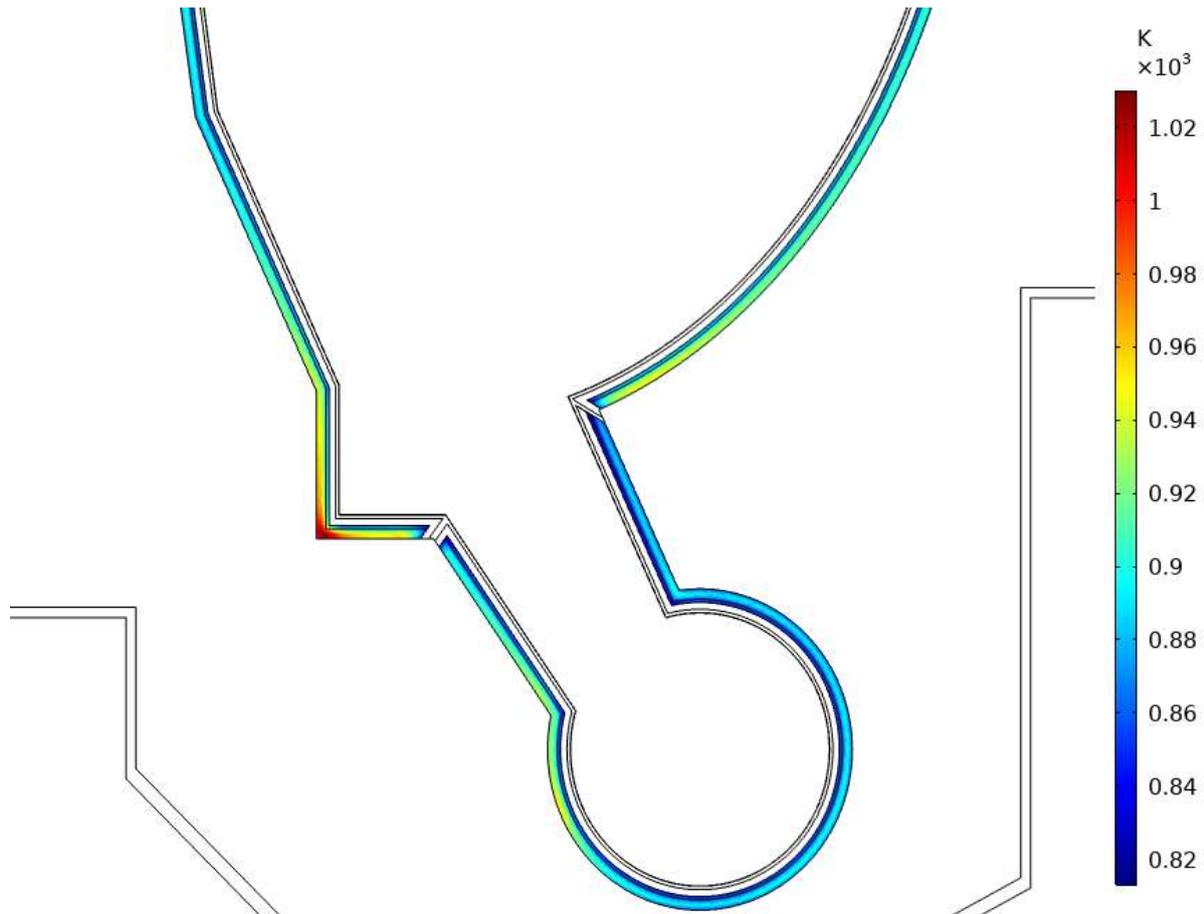
Figure 3.12 - Temperature distribution on Beryllium and Inconel (external) layers [Area D].

A model that couples both channel and tank can observe this phenomenon and identify critical spots due to it; if tank's convection is approximated with a constant temperature, the trend would be that outlet is the hottest spot and inlet is the coldest, without a current representation of the complexity that the geometry and tank's flow field represents (Figure 3.13).

Recirculating flows near vacuum vessel in the lower divertor region, where volumetric power generation is high, determine two hotspots with direct impact on vessel's temperature field. Moreover, FLiBe flowing through the channel is hotter near the outlet, impacting vessel's and tank's temperature in the same region: A small red (860 K) zone is located near the outlet on the central channel region, on the left of the plot. This hotspot is explained by recirculation and outlets as already observed, but also by the corner in the vacuum vessel geometry. Corners have a less efficient channel cooling resulting in hotspots in the solid layers.
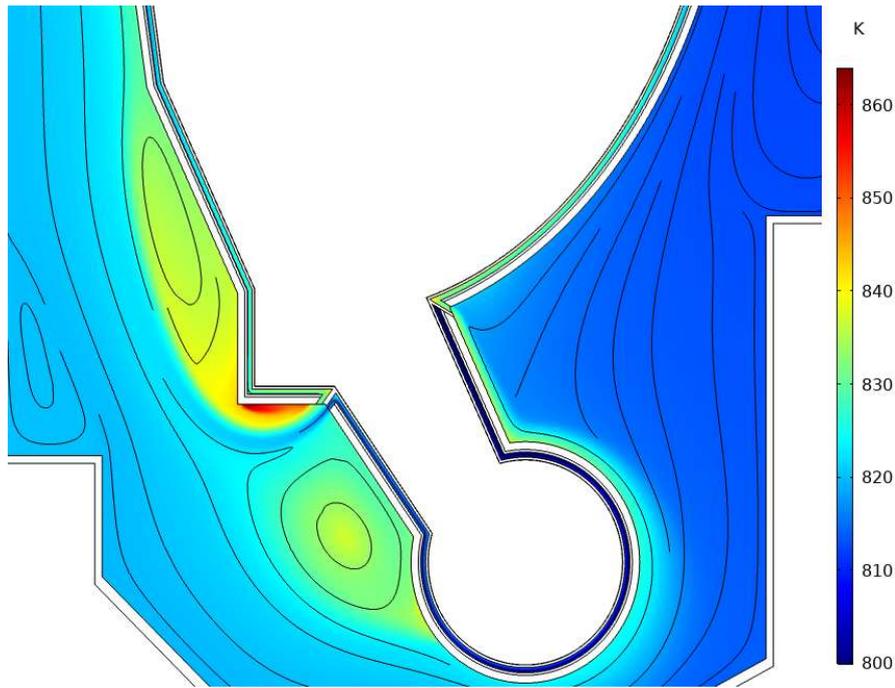
Figure 3.13 - Lower divertor tank's FLiBe temperatures [Area D].

FLiBe flowing from the channel is hotter than the average FLiBe temperature in the tank. Therefore, by joining the stream, channel flows heat up tank flow (Figure 3.13). However, FLiBe from the channel does not mix immediately with FLiBe in the tank, resulting in a how flow in the tank before mixing. Central channel, opposed to divertor channels, have the hottest FLiBe: in Figure 3.7 the two flowrates, coming from the two outlets one next to the other, seemed to mix immediately; however, temperature distribution highlights a different trend, as there are two different streams of different temperature for a big area before mixing happens (Figure 3.13, Figure 3.14).
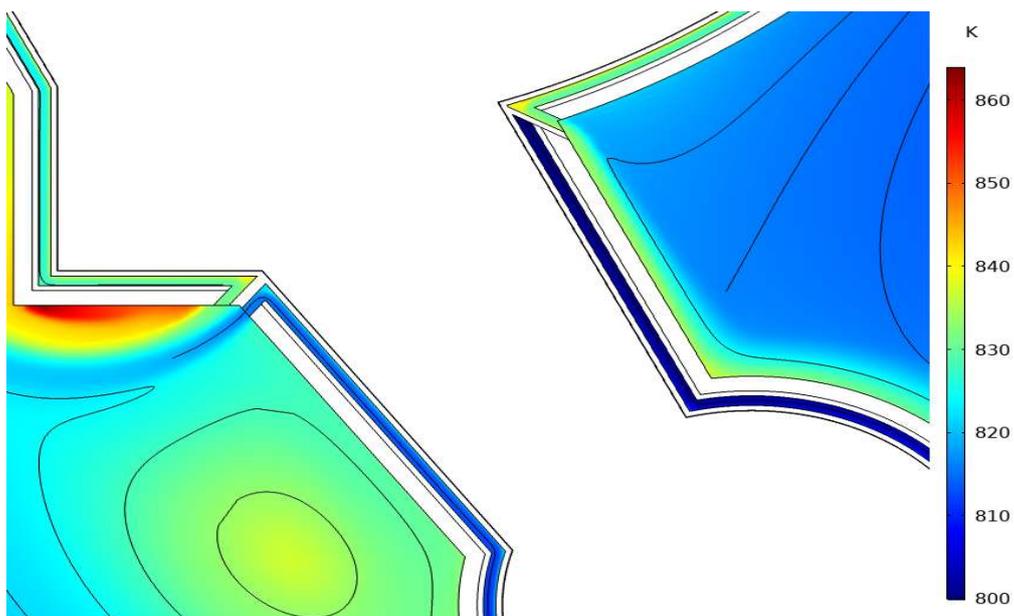
Figure 3.14 - Double outlet channel-tank Temperature distribution [Area F].

In the upper divertor region there are tank's auxiliary inlet, tank's outlet, and a big recirculation region towards one of the divertor's legs (Figure 3.15). Three peculiar areas with different temperature are one next to the others: tank's auxiliary inlet has the lowest temperature on the whole reactor, 800 K, and it dictates the whole reactor's temperature. Outlet temperature is 25 K hotter, which is FLiBe's average temperature on tank's outlet region. The hotspot is about 20 K hotter than outlet's temperature, and overall is one of FLiBe's hottest spots due to recirculation in ARC because of its position near the outlet. A mitigating factor in this recirculating flow's temperature is that it is located right where two vacuum vessel's channels' inlets are, reducing remarkably the temperature.
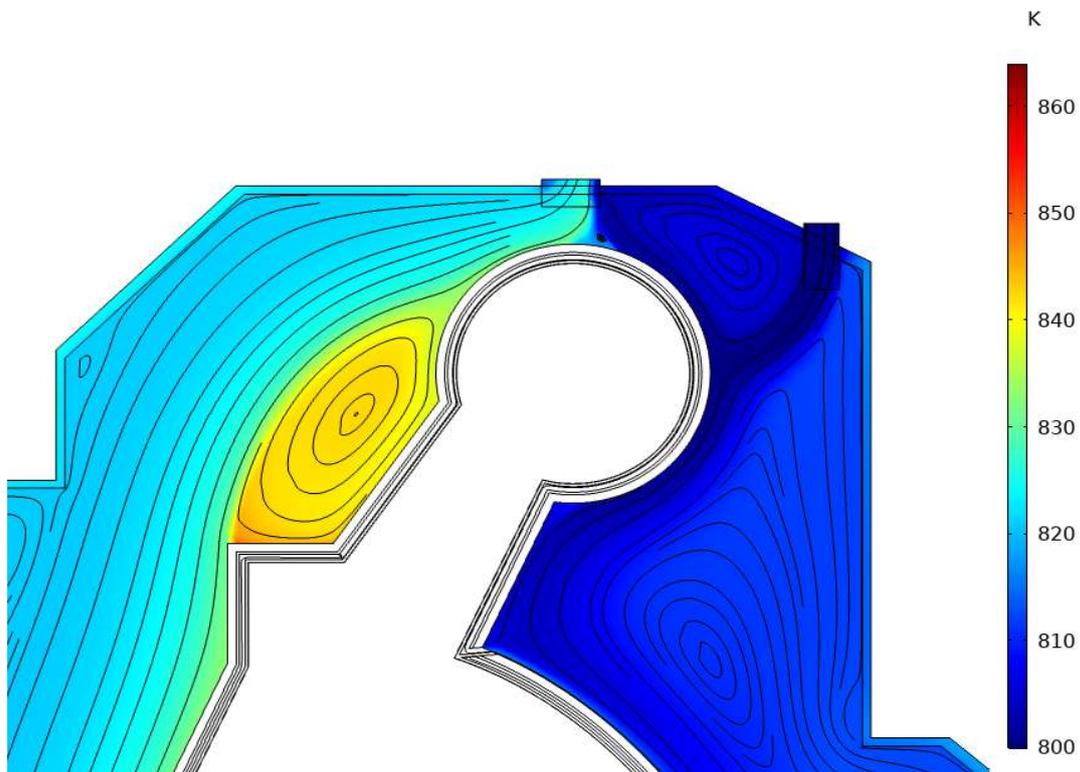
Figure 3.15 - Detail on upper divertor tank's temperature distribution [Area H].

Temperature field in external layers of the vacuum vessel in this region is affected by these peculiarities: hottest temperatures are, counterintuitively, near the inlets, due to tank's recirculating flow's influence (Figure 3.16). Tank's auxiliary inlet influences temperatures near the outlet region, which is among the coldest regions despite being near the outlet of the channel.
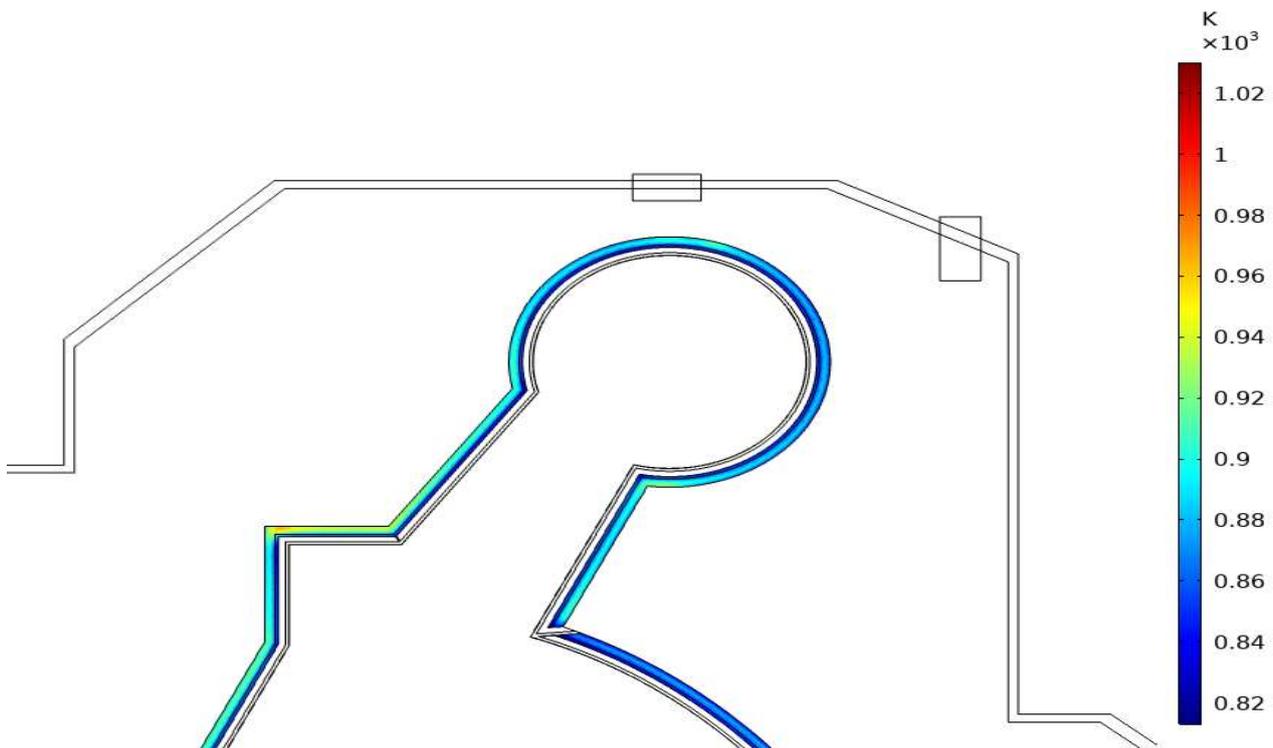
Figure 3.16- temperature distribution, external vacuum vessel's layers in upper divertor region [Area H].

3.3.3 Auxiliary tank's inlet analysis

A comparison between a geometry with auxiliary inlet and a geometry without is made in this section, explaining the reasonings for this new configuration. Simulations also highlighted that a configuration with an auxiliary inlet next to the outlet but on the inner side [9] is the same as a configuration without auxiliary inlets as the flowrate from the inlet flows directly into the outlet without considerable contribution in cooling the tank.

Without an auxiliary inlet for tank's region, the temperature gradient from inlet to outlet is bigger, due to lower FLiBe's flowrate in the tank. In fact, channel flowrates are limited by harsh velocity thresholds, which are not a limitation in tank region due to considerably different flow sections. A big recirculation region near the upper divertor, resulting in a big hotspot and a big criticality point (Figure 3.17). Moreover, no fresh FLiBe is coming to cool down tank's FLiBe, therefore the coolest point in tank region is channel outlet, which is already hot.
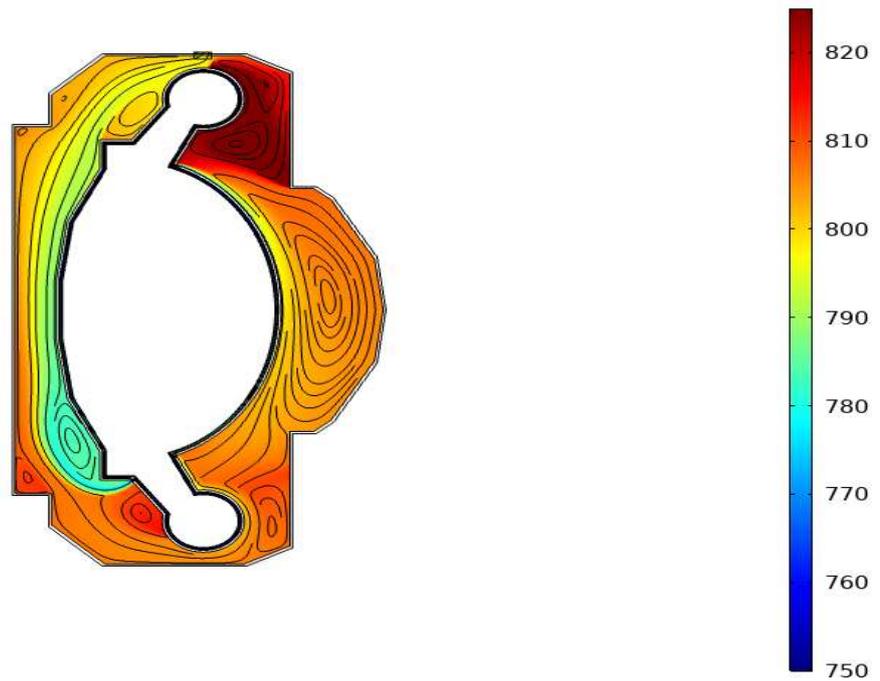
Figure 3.17 - ARC geometry without auxiliary inlet, Temperature field.

By following suggested inlets' configuration [9], fresh FLiBe coming from auxiliary inlet, positioned to the left of the outlet, would flow directly towards the outlet with scarce contribution, resulting in a similar scenario as Figure 3.17 displays. An auxiliary flowrate located on the outer side of the tank breaks recirculation and cools down the entire reactor (as shown in Figure 3.12). Auxiliary flowrate splits into two different flows, one of which going directly towards the outlet without contributing significantly to cooling (Figure 3.18); however, also this bifurcation can be helpful to prevent a recirculation between auxiliary inlet and outlet, where a critical hotspot (high power generation, near to the general outlet where temperatures are higher, corresponding to halfway of vessel's channel) can occur.
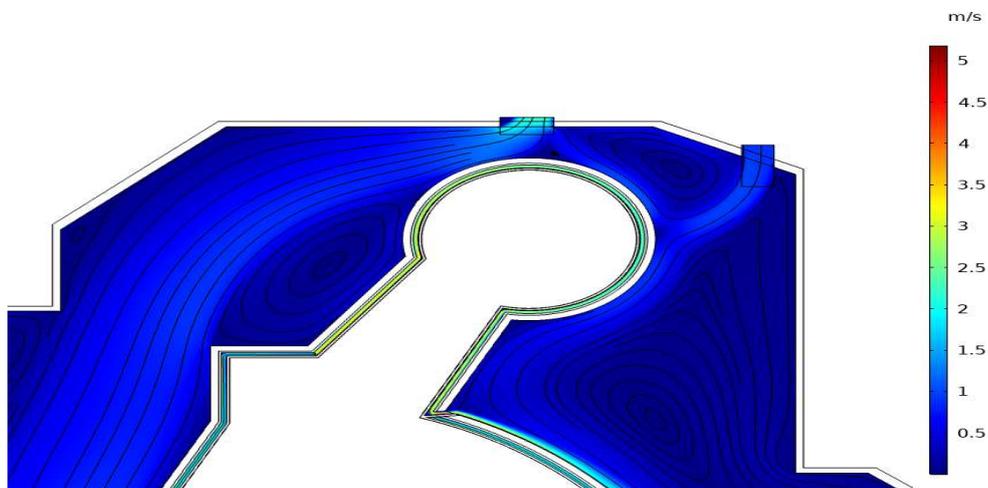
Figure 3.18 - Flow field near upper divertor region, with auxiliary inlet [Area H].

In Table 3.3, the average temperatures for each ARC materials are reported. Some considerations can be discussed by these results. It is evident how creep threshold of 930 K [10] for Inconel layers is not respected. Average Temperatures in ARC exceed the creep limit of 900 K. This is a consequence of high FLiBe's inlet temperature (800 K) and low heat transfer coefficient, as shown in Table 3.4.

Table 3.3 - ARC's average Temperatures for each material

ARC Average Temperatures	Value
Inlet blanket	800 K
Outlet blanket- divertor regions	816 K
Outlet blanket- central regions	832 K
Tank	834 K
First Wall	1210 K
Inconel- First layer	1090 K
Beryllium	860 K
Inconel- Second Layer	894 K
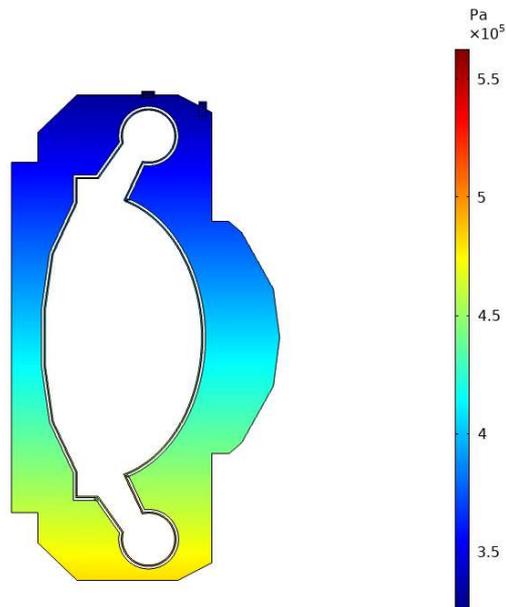
Figure 3.19 - ARC's pressure distribution.

ARC's pressure distribution is as expected to be (Figure 3.19). Setting an outlet pressure of 3 bar, it is possible to observe a pressure increase due to gravity. There are pressure drops in vacuum vessel's channel due to friction and turns (Figure 3.20). These pressure drops are displayed in Table 3.4.

Figure 3.20- Pressure losses in channel [D].

The CFD simulation for ARC made the estimate of some important results (Table 3.4), which are impossible to predict without a detailed simulation.

- ARC power is according to expected results.
- Average velocity in channel is not the threshold due to the acceleration phenomenon when FLiBe approaches the axis.
- Pressure drops from vacuum vessel to tank require a pumping power of 72.24 kW, a negligible fraction of reactor's electrical power output.
- The heat transfer coefficient in vacuum vessel's channel is lower than esteems, resulting in a vessel overheat. Increasing the heat transfer coefficient is a major concern, as velocity cannot be increased to enhance convection. A change in geometry can enhance the heat transfer coefficient, with the cost of increasing pressure drops, complexity in the vessel and solid material in the reactor.

Table 3.4 - ARC's simulation results

Main results	Value
Heat transfer coefficient - channel	5475 $W/m^2 \cdot K$
Pressure drops vessel-tank (average)	0.96 bar
Average velocity - tank	0.313 m/s
Average velocity - channel	1.98 m/s
Total reactor power	658 MW

4 Tritium Transport

4.1 Tritium Properties

Tritium is fundamental for fusion industry development and operation. Due to its relatively short half-life of 12.32 years, it is found in nature only in negligible amounts (due to cosmic rays). Nowadays, main Tritium producers are CANDU reactors, due to neutron irradiation of Deuterium in heavy water. The production in the world due to CANDU reactor's wastes is about $2\,kg/y$ [20], which is insufficient for fusion industry need.

To make fusion reaction economically feasible, Tritium production in situ is fundamental, because of scarce reserves and the expensive cost of Tritium ($30000\,\$/g$). Tritium can be produced with fast neutrons and Lithium:

$$^6Li + n = T + {}^4He + 4.8\,MeV$$

$$^7Li + n = T + {}^4He + n - 2.466\,MeV$$
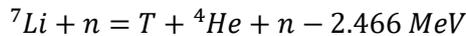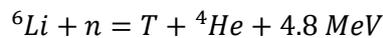
Neutron economy is fundamental for Tritium production in a blanket, and its most important indicator is the $TBR = \frac{Tritium\ produced\ in\ blanket}{Tritium\ burne\ \ in\ plasma}$, which must be larger than 1 for self-sufficiency. Each atom of Tritium burnt in plasma produces a neutron, which can be employed for Tritium production in blanket. Reactions involving [7]Li produce a Tritium atom and an additional neutron that can be consumed in [6]Li reaction. Because of neutron absorption by structural materials and neutron leakage, a neutron multiplier such as Beryllium is needed to furtherly enhance the TBR. In fact, TBR must be larger than one to take account of Tritium leakage, decay, and production for the startup inventory for another fusion reactor. While TBR=1.05 can be achieved with a great confidence, achievement of a TBR of 1.15 is uncertain [21].

Another important parameter in Tritium economy is the doubling time, the time employed to produce the startup inventory of the fusion reactor in addition to the Tritium used for normal operations. Tritium produced in the Breeding Blanket (BB) must be then extracted by the Tritium Extraction System (TES). TES has an extraction efficiency; therefore, a residual amount of Tritium remains solved in FLiBe, which is a major concern; because of its high permeability though most of metals, and the high compatibility with other elements (the same of H), Tritium can diffuse though the heat exchanger and pipes and reach the external environments. Tritium decay $T \rightarrow \beta^- + {}^3_2He$ produce β^- particles with average energy of 5.7 keV, therefore non-penetrating reactions. However, Tritium become hazardous when introduced in the body, by skin absorption, inhalation, ingestion. This can happen because Tritium may be present in tritiated water, dust particles, and gas. To reduce risk to workers and population, reduction of Tritium inventory and start up inventory is the most efficient way, because shielding and air filtration are not well suited for Tritium radiation- damage control [21].

4.2 Transport Phenomena

Tritium in a breeding blanket is present in many different forms, the principal being T_2 and TF [22]. A transport model of both species, including equilibrium between the two, must also include all fluorine chemical reactions with metal ions, corrosion induced phenomena and chemical models to compute. Therefore, a Tritium-only model will be analyzed as approximation. This approximation may be non-conservative because TF properties are different from T_2 and a study considering more species should be made.

Tritium transport is in a bulk fluid is influenced by diffusion and convective transport:

$$\frac{\delta c}{\delta t} - \nabla \cdot (D \nabla c) + \nabla \cdot (\boldsymbol{u} c) = R$$

Where c is the concentration in the considered domain, t is the time, D is the diffusion coefficient, u is the velocity vector and R is the reaction rate, therefore Tritium generation in $mol/m^3 s$

Tritium transport near a metal wall is influenced by dissociative absorption and recombinative desorption fluxes (Figure 4.1):

$$J_d = K_d P$$

$$J_r = K_r c^2$$

Where J_d is the dissociative adsorption flux, K_d is the dissociative adsorption constant, P is the partial pressure, J_r is the recombinative desorption flux, K_r is the recombinative desorption constant and c is the concentration.
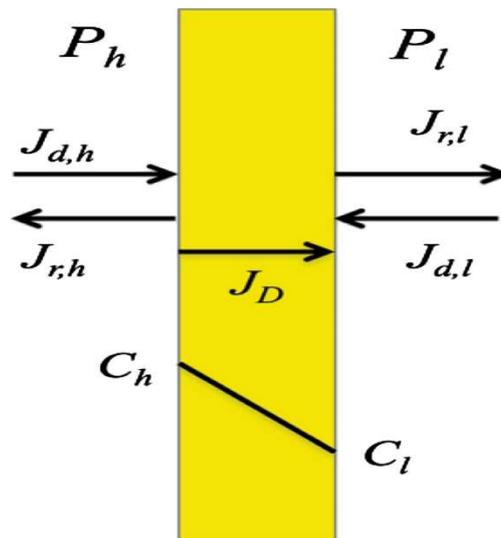
Figure 4.1 – Tritium fluxes involved in permeation through a metal membrane [21]*.*

In steady state condition recombinative and dissociative fluxes are in equilibrium:

$$K_d P = K_r c^2$$

Rearranging terms:

$$c = \sqrt{\frac{K_d}{K_r}} \sqrt{P} = K_s \sqrt{P}$$

Which is Sieverts' Law, being the Sieverts constant $K_s = \sqrt{\frac{K_d}{K_r}}$, and being c concentration of T.

In the steady state model that will be analyzed (Section 5.3) continuity of partial pressure through boundaries is assumed at the interface. In a liquid, therefore in FLiBe, partial pressure is evaluated through Henry Law:

$$c = kP$$

where k is the Henry coefficient and c is the concentration of T_2.

Henry coefficient, diffusion coefficient and Sievert coefficient are temperature dependent, usually in the form of an Arrhenius equation:

$$D = D_0 \exp\left(\frac{-E_D}{RT}\right)$$

$$K_S = K_{S,0} \exp\left(\frac{-E_S}{RT}\right)$$

$$k = k_0 \exp\left(\frac{-E}{RT}\right)$$

Where D_0, $K_{S,0}$, k_0 are pre-exponential factors E_D, E_S and E are activation energies dependent on the material and R is the universal gas constant.

Permeation flux though a membrane with high partial pressure and thickness l is described by Richardson Law:

$$J = \frac{\phi}{l} \cdot \left(\sqrt{P_h} - \sqrt{P_l}\right)$$

where P_h is the partial pressure on high concentration side, $P_l = 0$ is Tritium partial pressure outside the reactor, and the permeability is $\phi = DK_S$.

4.3   Transport physics

The *transport of diluted species* physic in COMSOL can compute transport and reaction of a specie dissolved in a liquid, in a gas or in a solid, if the concentration of the solute is orders of magnitude lower than the solvent one. This physics calculates transport by Fick's law, by convection for fluid media, and by migration in the presence of an electrical field [12]. The *transport of diluted species in porous media* is not suited for this simulation, as FLiBe does not flow inside vacuum vessel layers, and so does the *transport of concentrated species* physic interface, because of low concentrations involved.

In this case study, convection and diffusion are used for the model, and their check box in the options of the physic are filled, while migration will be neglected. Only one specie (T_2) is considered in the simulation, neglecting reactions between Tritium and other elements.

4.3.1   Transport properties

Diffusion coefficients in the physics are temperature dependent, and transport by convection is dependent on the velocity field. However, the physics can import velocity field and temperature field of a material under the domain condition *Transport Properties*, making possible a study without computing the non-isothermal flow once more, decreasing drastically computational cost. For solid materials, the velocity field must be specified as null to neglect the convective phenomena that are illogical. In the *Transport Properties* section diffusivities for each material are specified.

4.3.2   Inflow and outflow

Outflow condition is set on tank outlet. Inflow condition is a constant concentration profile:

$$c_{in} = \bar{c}_{out} \cdot (1 - \mu_{TE})$$

where μ_{TE} is Tritium Extraction system efficiency and $\bar{c}_{out}$ is the average outlet concentration. This boundary condition is applied to each inlet of the configuration shown in Chapter 3.

4.3.3 Tritium generation

One fundamental information is the Tritium generation, which can be modelled in the *Reactions* domain condition. This condition set a value for the parameter R in the equation $\nabla J + u \cdot \nabla c = R + S$. Tritium generation in Inconel 718, Tungsten and Beryllium is neglected. Tritium generation in vacuum vessel channel is set constant, $R_{chann} = 9.88\,E - 6\; mol/m^3 s$. This value is obtained by adapting a Tritium generation shape with a coefficient to match Tritium production (evaluated *a posteriori* by integrating in all domains) according to a plasma power of 525MW and a TBR=1.06. Tritium generation in tank is modelled from the same basis as power generation (Section 3.2.2) with a negative exponential profile from neutronic calculations [13] (Figure 4.2). Tritium generation is halved considering that the specie c in FLiBe is T_2 and not T.
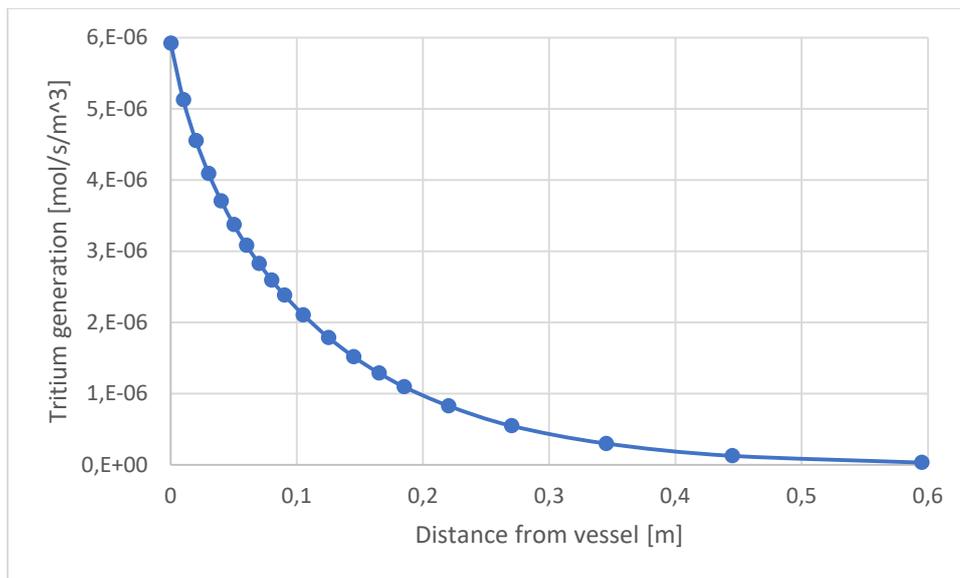
Figure 4.2 - Tritium production profile in tank FLiBe

4.3.4 Partition condition

Partition condition is fundamental in this model to determine concentration in solid materials. This condition can be used in a steady state solution to keep partial pressure continuity. A time dependent model would compute recombinative and dissociative fluxes, which in this model are simplified by Sieverts law and Henry law with partial pressure continuity condition.

In COMSOL Multiphysics a partition condition set a ratio between the concentration on one side of the interface and the concentration on the other side. To set a partition condition there is a direction shown by an arrow to distinguish c_u and c_d (concentration up and down), being c_u pointed by the arrow and $partition = \frac{c_u}{c_d}$. Due to the complex geometry, the software tool may reverse the direction arrow after sharp turns, making necessary a particular attention on the direction for each boundary.

Solid-Solid Interface partition condition

To keep continuity in partial pressure the partition condition between two solids (Tungsten and Inconel 718) is set as the ratio between Sievert constants:

$$p_{partial,W} = \left(\frac{c_W}{k_{s,W}}\right)^2$$

$$p_{partial,\text{Inc}} = \left(\frac{c_{\text{Inc}}}{k_{s,\text{Inc}}}\right)^2$$

$$\frac{c_{Inc}}{c_W} = \frac{k_{s,Inc}}{k_{s,W}}$$

where c_W is the concentration in Tungsten, c_{Inc} is the concentration in Inconel 718, $p_{partial}$ is Tritium partial pressure in the Tungsten or Inconel, $k_{s,W}$ is the Sieverts' constant for Tungsten and $k_{s,\text{Inc}}$ for Inconel.

The same partition condition is applied to Beryllium-Inconel Interface.

Fluid-Solid Interface partition condition

Partition condition between solid and fluid (FLiBe and Inconel) is set to keep continuity in partial pressure:

$$p_{partial,\text{Inc}} = \left(\frac{c_{\text{Inc}}}{k_{s,\text{Inc}}}\right)^2$$

$$p_{partial,\text{FLiBe}} = \frac{c_{FLiBe}}{k_{henry}}$$

$$\frac{c_{FLiBe}}{c_{Inc}} = \frac{c_{Inc} \cdot k_{henry}}{k_{s,\text{Inc}}^2}$$

The same condition is applied in the Beryllium-FLiBe interface.

4.3.5 *No Flux* boundary condition

No flux condition is applied to Tungsten-Plasma boundary.

A *No flux* condition is applied to Inconel 718 shell external boundary, as a conservative approximation. Consistent stabilization techniques such as crosswind diffusion (Do Carmo and Galeão [12]) and streamline diffusion are set as default.

4.3.6 Transport properties

Transport properties, including temperature dependences and their sources, are displayed in Table 4.1. Diffusion coefficients for Inconel 718[23] and Beryllium[24] are adapted from Deuterium to Tritium by multiplying them with the factor $\sqrt[2]{m_D/m_T}$. However, Sieverts' and Henry's constant are the same for the two isotopes [25].

Table 4.1 - Transport property correlation for ARC materials.

Material	Diffusion coefficient $[m^2/s]$	Sieverts' and Henry's constant
Inconel 718 [23]	$10^{\left(-5.98-\left(\frac{0.52\ eV/mol}{2.303\cdot R\cdot T}\right)\right)}$	$\phi_{Inc} = 10^{\left(-7.04-\left(\frac{0.55\ eV}{2.303\cdot k_B\cdot T}\right)\right)} mol/m\cdot s\cdot Pa$ $k_{S,Inc} = \frac{\phi_{Inc}}{D_{Inc}}$
FLiBe [26]	$9.3E-7 exp\left(\frac{-43E3\ J/mol}{R\cdot T}\right)$	$k_h = 7.9E-2 exp\left(\frac{-35E3\ J/mol}{R\cdot T}\right) mol/m^3 Pa^{1/2}$
Tungsten [27]	$4.1E-7 exp\left(\frac{-0.37\ eV}{k_B\cdot T}\right)$	$k_{S,W} = \frac{1.83E24\ exp\left(\frac{-1.04\ J}{k_B\cdot T}\right)}{N_A} mol/m^3 Pa^{1/2}$

| Beryllium [24] | $8E - 9exp\left(\dfrac{-3.5E4\,^{J}/_{mol}}{R \cdot T}\right)$ | $k_{S,Be} = \dfrac{1.1E21 \exp\left(\dfrac{-1.8E3\,J}{R \cdot T}\right)}{N_A} mol/m^3 Pa^{1/2}$ |

4.4 Study

Stationary study is made for Tritium transport. Non-isothermal flow is enabled in the study, but not solved by the solver. Initial conditions from a previous solution are set for transport variables to decrease computational cost. The initial condition for the first study was $1E - 8\,^{mol}/_{m^3}$ for each domain. Initial conditions for variables not solved by the solver (non-isothermal flow variables) are set from the CFD model solution. Direct solver PARDISO [12] with tolerance of 0.02 is used for this simulation.

5   Concentration field Results

5.1   Mesh convergence analysis

To verify the results shown in Section 5.2, a mesh convergence study on the Tritium transport model has been carried; results have shown a good mesh for Beryllium, Tungsten, Inconel vessel and FLiBe channel, with a relative error below 5% (Figure 5.1). Inconel shell results show an error of 6.35% for the finest mesh, but being the domain with the coarsest mesh, further mesh refinements do not represent a computational burden. GCI for FLiBe tank concentration did not meet expected results below 5%. Tank mesh is already a high computational burden as it is the biggest meshed area in the model with the finest mesh size of 0.76 mm. Further mesh refinements on FLiBe tank are needed, but they are impossible to carry due to computational limits. Initial data and results for mesh convergence are reported in Appendix C.
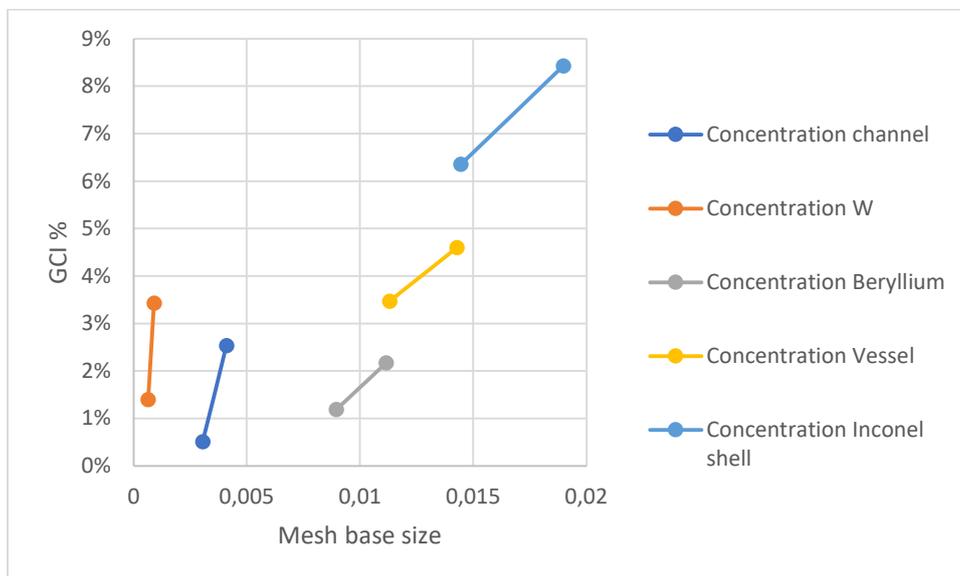
Figure 5.1 - Mesh convergence GCI% results for transport model

Converged mesh has 1279196 elements, with average element quality of 0.889 and minimum mesh quality of 0.046. Base size for each material is reported in Table 5.1.

Table 5.1 - Converged mesh base size foe each domain

Domain	h
Channel	0,003043
Tank	0,007564
W	6,35E-04
Be	8,94E-03
Vessel	0,008001
Shell	0,010351

5.2   Concentration field results

In steady state condition, the concentration strongly depends on partial pressure, which is set in FLiBe by inlet condition and Tritium generation, and on material properties; Sievert and Henry coefficients (Table 5.3)

influence the average concentration, which can vary by several orders of magnitude while keeping partial pressure continuity. Because of its high Sievert coefficient, Tritium concentration in Inconel 718 is three orders of magnitude higher than every other, contributing almost alone to the inventory (Table 5.2). The other significant contribution, from tank FLiBe, is the 14.5% of the total inventory, which is $1.86\ g$. Concentration in FLiBe domains is concentration of T_2, therefore it is multiplied by the coefficient $6\ g/mol$, while concentration in solid materials is T concentration with molar mass $3\ g/mol$.

Table 5.2 - Tritium concentration and Inventory in ARC.

Domain	Inventory $[mol]$	Average concentration $[mol/m^3]$
FLiBe channel	1.05E-4	1.36E-5
FLiBe Tank	0.05	1.56E-4
Inconel 718 Vessel	0.23	1.49E-2
Inconel 718 tank shell	0.30	2.00E-2
Tungsten	9.77E-6	2.57E-5
Beryllium	1.26E-3	3.32E-4

Table 5.3 - Transport properties of ARC materials.

Domain	Diffusivity $[m^2/s]$	K Sievert / K Henry
FLiBe	1.9E-9	$k_{henry.FLiBe} = 4.54E-4\ mol/m^3 \cdot Pa$
Tungsten	1.18E-8	$k_{S,W} = 1.5E-4\ mol/m^3 Pa^{1/2}$
Beryllium	5.9E-11	$k_{S,Be} = 0.0015\ mol/m^3 Pa^{1/2}$
Inconel 718	1.3E-9	$k_{S,Inc} = 0.058\ mol/m^3 Pa^{1/2}$

Tritium generation is the main driver in concentration field for the entire reactor, while inlet concentration condition has a smaller influence. Tritium concentration in FLiBe is responsible for concentration in other materials, therefore it is important to analyze phenomena that can change it significantly.

Concentration in vacuum vessel channel is lower as the minimum concentration is located into the inlet ($c_{in} = 7.22E-6\ mol/m^3$), but also because there is almost no recirculating flow in the channel. In fact, in recirculating flows, concentration rises significantly, except in low Tritium generation areas where this phenomenon is softened (Figure 5.2). Outlet average concentration $c_{out} = 3.61E-5\ mol/m^3$ is significantly lower than tank average concentration because recirculating flows significantly increases the average both because of magnitude and dimension. In the tank flow going through the tank, concentration is visibly lower (Figure 5.3).
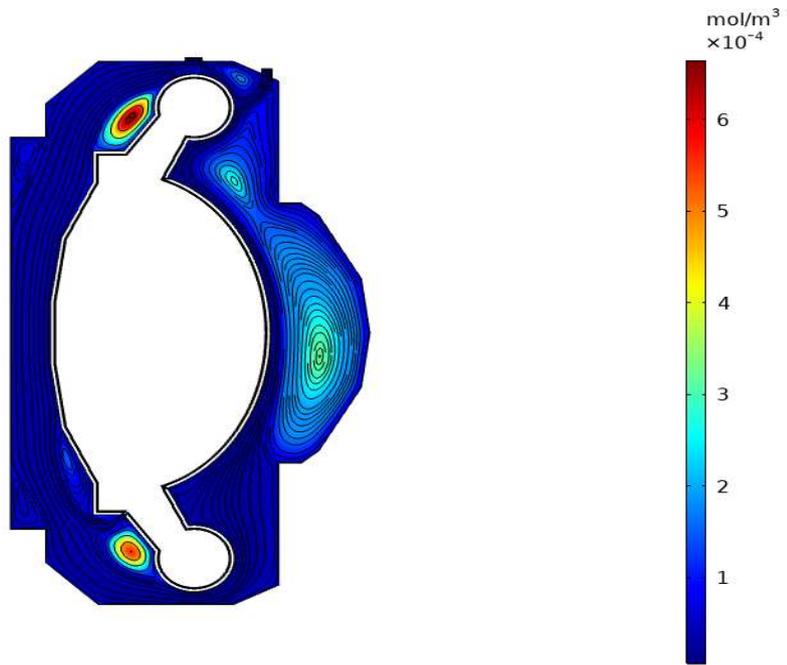
Figure 5.2 - ARC concentration distribution in FLiBe.
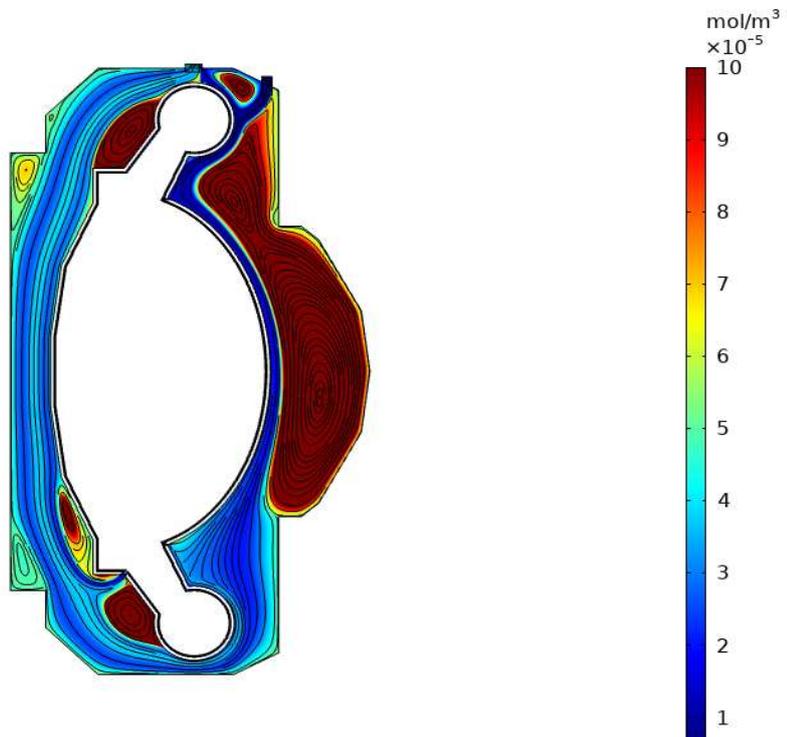
Figure 5.3 - ARC concentration distribution in FLiBe with rearranged color scale.

Tritium leakage is directly dependent on concentration in the layer, and the presence of many recirculating flows in proximity to the external Inconel 718 shell increase both. Corners in tank can be rounded to prevent leakage enhancing, and the great recirculating flow in the central region can induce a criticality.

A *Flux* condition can be applied to tank shell external boundary to simulate Tritium leakage due to diffusion. Simulations evidenced no significant difference between the *No Flux* solution because of the low magnitude of the flux compared to concentration in the layer. The flux can be evaluated by Richardson equation [21]. Tritium leakage in steady state condition (which is the maximum inventory condition for FLiBe breeding blanket) is estimated to be $3.37E - 8 \, mol/s$. A preliminary estimation in terms of dose has been carried out. For a full power year with availability factor of 80% (which will be needed in commercial power plants) estimated leakage is about 1.79 mSv, which is over the US DOE guidance on Tritium handling and storage limit for normal operations ($0.1 \, mSv/y$)[21].

6 Conclusions and future perspectives

CFD and Tritium transport steady-state models for ARC have been performed with COMSOL Multiphysics. A multiphysics model which couples thermal, fluid dynamic and transport physics had been developed, considering the influence of each physics from the others. Indeed, velocity, temperature, and concentration fields have been determined for ARC reactor. Results for both simulations are consistent with ARC literature. Observed results underlined criticalities such as:

- Low heat transfer coefficient in vacuum vessel channel, 5470 $W/(m^2 \cdot K)$ of the needed value of 40-50 $kW/(m^2 \cdot K)$. New channel design should be tested to improve heat transfer;
- Large eddies in tank flow field, which can provoke high thermal excursions;
- High temperature (1090 K) for inner Inconel 718 layer, which overcomes the creep limit of 930 K [10][28];
- Velocity distribution that can overcome corrosion threshold of 2.7 m/s in localized points, in particular the outlet of the low divertor channel;
- High Tritium concentration in Inconel 718, which is orders of magnitude higher than the one of the others' and has a contribution of over 85% in Tritium inventory.

The models analyzed in this thesis work include a complete CFD model of a real 2D ARC geometry and a transport model built on results of CFD model, with complex flow field, temperature field and geometry. The models include an elaborated inlet configuration, power and tritium generation profiles, realizable k-Ɛ turbulence model and a mesh convergence study for CFD model. However, analyzed models have some approximations and limits such as:

- No plasma heat flux distribution on the first wall, leading to localized hotspots where probably the heat flux is lower;
- No realistic inlet pipes because of 2D symmetry, inlets are ring-shaped;
- No MHD effects;
- High uncertainty of measures on Tritium transport properties in some materials and for hydrogen isotopes, which can drastically influence transport model;
- High tolerance and computational cost on transport model due to complexity and size of the computational domain;
- No considerations on Tritium chemical reactions.

The developed models in this thesis work represent a starting point for further analysis:

- Different inlet configurations can be tested by modifying geometry and different flowrate inlet condition can be tested by modifying inlet boundary conditions. Inlet conditions can have a major impact on FLiBe eddies and in minimum/maximum velocity ratio in FLiBe channel;
- Recent literature is considering different candidates for Inconel 718 due to high activation under neutron irradiation. Different materials, such as Vanadium alloys and high-entropy alloys, can be tested both for CFD and transport simulations, to observe critical temperatures and Tritium concentration.
- Time-dependent study for CFD model can be implemented by adding a time dependent variable to simulate pulsed power generation. A time-dependent model can give important information on startup and shutdown transients, and how much time it takes to reach steady state;

- Time-dependent study for Tritium transport can be implemented by adding a time dependent variable for Tritium production and simulating recombinative and dissociative Tritium flux instead of using a partition conditions; this model is important to evaluate the startup inventory when Tritium concentration in the reactor is zero and the amount of extracted Tritium is lowered by materials absorbing it to build up a steady-state concentration.

It seems that ARC reactor is one of the fastest and cheapest routes to achieve fusion power plants, with innovative and simple design and with a reduced size. Research is the backbone for the development of this technology, and it has achieved several results; however, many technological challenges are yet to be overcome, and research is still lacking on some critical aspects like transport properties of Tritium and its derivates (like TF) in different materials (Tritium experiments are very hard, due to radiological risks, and very expensive to do) and molten salt corrosion on structural materials. These two aspects, combined with a deep analysis on Tritium reactions with other elements in ARC reactors, will have a big impact on one of the most critical challenge for fusion reactors, which is Tritium breeding and extraction.

7 Bibliography

[1] J. Freidberg, "Plasma Physics and Fusion Energy," *Cambridge Univ. Press.*, 2007. doi:10.1017/CBO9780511755705.

[2] S. Segantin, R. Testoni, and M. Zucchetti, "The lifetime determination of ARC reactor as a load-following plant in the energy framework," *Energy Policy*, vol. 126, no. October 2018, pp. 66–75, 2019, doi: 10.1016/j.enpol.2018.11.010.

[3] R. Aymar ,P. Barabaschi, Y. Shimomura, "The ITER Design," *Plasma Phys. Control Fusion 44*, vol. 1, pp. 519–565, 2002.

[4] S. Konishi, S. Nishio, and K. Tobita, "DEMO plant design beyond ITER," *Fusion Eng. Des.*, vol. 63–64, pp. 11–17, 2002, doi: 10.1016/S0920-3796(02)00264-8.

[5] B. N. Sorbom, J. Ball, T. R. Palmer, F. J. Mangiarotti, J. M. Sierchio, P. Bonoli, C. Kasten, D. A. Sutherland, H. S. Barnard, C. B. Haakonsen, J. Goh, C. Sung, D.G. Whyte, "ARC: A compact, high-field, fusion nuclear science facility and demonstration power plant with demountable magnets," *Fusion Eng. Des.*, vol. 100, pp. 378–405, 2015, doi: 10.1016/j.fusengdes.2015.07.008.

[6] F. Wagner, "Fusion energy," MRS Energy & Sustainability, 5, pp. 1–16, 2018, doi: 10.1557/mre.2018.8.

[7] G. Neilson, "Magnetic Fusion Energy : From Experiments to Power Plants," *Elsevier Sci. Technol.*, 2016.

[8] M. Greenwald, D. Whyte, P. Bonoli, Z. Hartwig, J. Irby, B. Labombard, E. Marmar, J. Minervini, M. Takayasu, J. Terry, R. Vieira, A. White, S. Wukitch, D. Brunner, R. Mumgaard, B. Sorbom, "The High-Field Path to Practical Fusion Energy," 2017.

[9] A. Q. Kuang, N. M. Cao, A. J. Creely, C. A. Dennett, J. Hecla, B. LaBombard, R. A. Tinguely, E. A. Tolman, H. Hoffman, M. Major, J. Ruiz, D. Brunner, P. Grover, C. Laughman, B. N. Sorbom, D.G. Whyte, "Conceptual design study for heat exhaust management in the ARC fusion pilot plant," *Fusion Eng. Des.*, vol. 137, no. August, pp. 221–242, 2018, doi: 10.1016/j.fusengdes.2018.09.007.

[10] S. Segantin, " Load following Concept Feasibility of ARC Reactor Power Plant Based on Thermo-mechanical Analysis of the Vacuum Vessel" 2017.(Master thesis, Politecnico di Torino)

[11] A. Aimetta, "Neutronic analysis of the fusion reactor ARC : Monte Carlo simulations with the Serpent code,". Nov. 2020. doi: 10.5281/zenodo.4292229. url: https://doi.org/10.5281/zenodo.4292229. (Master thesis, Politecnico di Torino)

[12] "COMSOL Multiphysics® v. 5.4." Stockholm, Sweden, www.comsol.com.

[13] R. Testoni, S. Segantin, and S. Meschini, "Internal Report: WP2 : Tritium Transport," 2020.

[14] S. Segantin, R. Testoni, Z. Hartwig, D. Whyte, and M. Zucchetti, "Exploration of a Fast Pathway to Nuclear Fusion: Thermal Analysis and Cooling Design Considerations for the ARC Reactor," *Fusion Sci. Technol.*, vol. 76, no. 1, pp. 45–52, 2020, doi: 10.1080/15361055.2019.1629252.

[15] P.J. Karditsas, M. J. Baptiste. "Thermal and structural properties of fusion related materials", (UKAEA-FUS--294). United Kingdom 1995.

[16] S. Cantor, "Density and Viscosity of Several Molten Fluoride Mixtures," ORNL, ORNL-TM-43, 1973.

[17] P. K. Romano, N. E. Horelik, B. R. Herman, A. G. Nelson, B. Forget, and K. Smith, "OpenMC: A state-of-the-art Monte Carlo code for research and development," *Ann. Nucl. Energy*, vol. 82, pp. 90–97, 2015, doi: 10.1016/j.anucene.2014.07.048.

[18] P. J. Roache, "Quantification of uncertainty in computational fluid dynamics," *Annu. Rev. Fluid Mech.*,

vol. 29, pp. 123–160, 1997, doi: 10.1146/annurev.fluid.29.1.123.

[19] W. L. Oberkampf and C. J. Roy, "Verification and Validation in Scientific Computing.", 2010th ed. New York: *Cambridge University Press*, 2018.

[20] P. Gierszewski, "Tritium supply for Near-term fusion devices," *Fusion Engineering and Design*, vol. 10,1989, pp. 399–403.

[21] M. Abdou,M. Riva, A. Ying, C. Day, A. Loarte, L.R. Baylor, P. Humrickhouse, T. F. Fuerst, S. Cho, "Physics and technology considerations for the deuterium-tritium fuel cycle and conditions for tritium fuel self sufficiency," *Nucl. Fusion*, vol. 61, no. 1, 2021, doi: 10.1088/1741-4326/abbf35.

[22] J. D. Stempien, R. G. Ballinger, and C. W. Forsberg, "An integrated model of tritium transport and corrosion in Fluoride Salt-Cooled High-Temperature Reactors (FHRs) – Part I : Theory and benchmarking," *Nucl. Eng. Des.*, vol. 310, pp. 258–272, 2016, doi: 10.1016/j.nucengdes.2016.10.051.

[23] D. J. Mitchell and E. M. Edge, "Permeation characteristics of some iron and nickel based alloys," *J. Appl. Phys.*, vol. 57, no. 12, pp. 5226–5235, 1985, doi: 10.1063/1.335261.

[24] E. Abramov, M. P. Riehm, D. A. Thompson, and W. W. Smeltzer, "Deuterium permeation and diffusion in high-purity beryllium," *J. Nucl. Mater.*, vol. 175, no. 1–2, pp. 90–95, 1990, doi: 10.1016/0022-3115(90)90274-Q.

[25] C. S. Marchi, B. P. Somerday, and S. L. Robinson, "Permeability, solubility and diffusivity of hydrogen isotopes in stainless steels at high gas pressures," *Int. J. Hydrogen Energy*, vol. 32, no. 1, pp. 100–116, 2007, doi: 10.1016/j.ijhydene.2006.05.008.

[26] P. Calderoni, P. Sharpe, M. Hara, and Y. Oya, "Measurement of tritium permeation in flibe (2LiF-BeF2)," *Fusion Eng. Des.*, vol. 83, no. 7–9, pp. 1331–1334, 2008, doi: 10.1016/j.fusengdes.2008.05.016.

[27] H. Nakamura, S. Sakurai, S. Suzuki, T. Hayashi, M. Enoeda, and K. Tobita, "Case study on tritium inventory in the fusion DEMO plant at JAERI," *Fusion Eng. Des.*, vol. 81, no. 8-14 PART B, pp. 1339–1345, 2006, doi: 10.1016/j.fusengdes.2005.10.009.

[28] C. Bast, "Probabilistic material strength degradation model for Inconel 718 components subjected to high temperature, mechanical fatigue, creep and thermal fatigue effects," *NASA Rep.*, 1994.

APPENDIX A

Mesh Convergence data- CFD Model

In the Tables A.1, A.2, A.3, and A.4, results from COMSOL simulation are shown for different mesh, with a sequential mesh refinement on the entire ARC mesh for the CFD model.

Table A.1 - Coarsest mesh GCI data

Channel								Tank		
T ave	dp ave	h	v ave	T W ave	T be ave	T inner inc ave	T outer inc ave	T ave tank	h tank	v ave tank
813,279343	96184,174494	0,006363	1,983041	1211,371319	859,299739	1092,173344	896,090866	834,100597	0,010667	0,319232

Table A.2 - Intermediate mesh GCI data

Channel								Tank		
Tave	dp ave	h	v ave	T W ave	T be ave	T inner inc ave	T outer inc ave	T ave tank	h tank	v ave tank
813,317270	96159,169098	0,004623	1,984621	1210,214195	858,978534	1090,836159	897,070189	834,040549	0,007562	0,321361

Table A.3 - Finest mesh GCI data

Channel								Tank		
Tave	dp ave	h	v ave	T W ave	T be ave	T inner inc ave	T outer inc ave	T ave tank	h tank	v ave tank
813,297263	97433,182944	0,003344	1,986663	1208,682618	8,581065	1089,326808	897,036514	833,983694	0,005351	0,327091

Table A.4 – Mesh convergence

	Tave channel	dp ave	v ave channel	T W ave	T be ave	T inner inc ave	T outer inc ave	T ave tank	v ave tank
p	-2	2	3	0.454282	2	0.577	2	3	3
GCI fine	010.0729	34	0.002336	9	0.452626	8	2	0	0.001455
GCI Coarse	0.05332	65	0.004311	11	0.854132	10	4	0	0.004117
GCI % fine	-1.09E-04	5.04E-04	0.001177	0.007651	5.27E-04	0.007566	0.00182	5,65E-05	0.004529
GCI % Coarse	-5.39E-05	8.57E-04	0.002469	0.008914	0.00113	0.009187	0.003643	1,44E-04	0.012647

Appendix B

Mesh convergence data- CFD Model channel

In the Tables B.1, and B.2, results from COMSOL simulation are shown for different mesh, with a sequential mesh refinement focused on the channel mesh for the CFD model. In Table B2 results for maximum temperature gave infinite as order of convergence because the difference between the second order value and the third order value is 3E-12 (for this reason p is equal to infinite).

Table B.1 - Grid convergence initial data for meshes with different refinement order.

Mesh order	T ave	Mesh size	v ave	T max	v max
1	813.1986	0.00210823	1.988451	885.5031	5.77031404
2	813.3123	0.00172727	1.988348	894.1858	5.77632932
3	813.3209	0.00108632	1.986915	894.1858	5.76793302

Table B.2- Grid convergence results

	T ave	Mesh size	V ave	T max	V max
p	13	0.0017273	-5	inf	3
GCI fine	2.27E-05	0.0021082	0.00199701	0	0.404149891
GCI Coarse	0.010799	0.0010863	2.06E-04	0,00000000	1
GCI % fine	2.79E-08		0.001	0,00E+00	0.070068409
GCI % Coarse	3.68E-07		7.19E-04	0	0.081080594

Appendix C

Mesh convergence data- Tritium transport Model

In the following Tables results from COMSOL simulation are shown for different mesh, with a sequential mesh refinement for the Tritium transport model. h is mesh base size , C is the average concentration evaluated in the domain. In Table C.2 results for tank mesh convergence are unreliable, as they have not yet reached convergence (p=0.14). Results for Inconel external shell show an error of 6.3% which is higher than the highest desired error to consider reliable results in this work (5 %).

Table C.1 – Grid convergence data for COMSOL transport model

	Channel		Tank		Be		W		Vessel		Shell	
Order	h	C	h	C	h	C	h	C	h	C	h	C
1	0,004097	1,36E-05	0,014984	1,27E-04	0,011145	3,33E-04	9,02E-04	2,55E-05	0,014274	0,014956	0,018967	0,019647
2	0,003043	1,39E-05	0,010667	1,79E-04	8,94E-03	3,45E-04	6,35E-04	2,63E-05	0,011298	0,015632	0,014437	0,021225
3	0,002349	1,40E-05	0,007564	2,29E-04	0,006533	3,52E-04	4,62E-04	2,66E-05	0,008001	0,016159	0,010351	0,022025

Table C.2 Grid convergence results for COMSOL Tritium transport model

	C channel	C Tank	C W	C Be	C vessel	C shell
p	5,17942	0,13792	2,33325	3,59959	2,25216	1,48958
GCI fine	1,21E-07	0,001285	3,71E-07	1,29E-05	5,60E-04	0,001027
GCI Coarse	3,15E-08	0,001348	7,81E-07	4,18E-06	0,001219	0,001685
GCI % fine	0,005087	5,60928	0,01396	0,011866	0,034684	0,06353
GCI % Coarse	0,025364	7,43166	0,034248	0,021681	0,046001	0,084259